DYNAMIC ^{31}P MRS WITH A 1 TELSA EXTREMITY SCANNER

A Thesis

by

MINYU GU

Submitted to the Office of Graduate and Professional Studies of

Texas A&M University

in partial fulfillment of the requirements for the degree of

MASTER OF SCIENCE

Chair of Committee,	Steven M. Wright
Committee Members,	Jim Ji
	Mary P. McDougall
	Robert D. Nevels
Head of Department,	Miroslav M. Begovic

August 2019

Major Subject: Electrical Engineering

ABSTRACT

^{31}P MRS offers unique non-invasive access to investigate the in vivo metabolism and is a significant advancement in the understanding and treating of many disease processes. The challenge of in vivo dynamic ^{31}P MRS mainly originates from the relatively low concentration of phosphorus and the requirement of static magnetic field's high homogeneity to distinguish the chemical shift of the peaks. Hence, conventional ^{31}P MRS is usually done in the high field / ultra-high field whole-body MRI system equipped with multiple channels B_0 shimming coil. On the other hand, extremity NMR scanners which usually have low (<0.5T) or medium (0.5-1T) field strength are often available for a relatively low cost. Those limitations make high temporal resolution dynamic ^{31}P MRS difficulty using conventional NMR signal acquisition technology in extremity NMR scanners.

We propose here using a four-element coil receive-only array and a transmit-only birdcage to investigate the possibility of dynamic ^{31}P MRS in a 1T ONI extremity scanner. NMR phased array simultaneously acquires multiple channels' signal from non-interacting receive coils array and subsequently combines the data. In the condition of a poor shimming magnet, another improvement of spectral peak linewidth by replacing single channels coil with multiple smaller channels coils is also studied. A legible spectral is obtained from in vivo volunteers with 4-16 averages, which gives us 16s-64s temporal resolution. The array coil combined SNR is found to be 1.8 times better than using a single loop as a receive coil of the same overall size, and linewidth is improved from 0.72 to 0.45 ppm. This platform shows the potential for monitoring ^{31}P in vivo metabolism with meaningful temporal resolution in an easy instrument outside of the hospital environment.

ACKNOWLEDGEMENTS

First, I would like to thank my committee chair, Dr. Wright. He has been a great advisor and led me into the field of NMR. His intelligence inspires many work of mine and shows me how to turn impossible tasks into possible.

Thanks also go to my friends and colleagues at Texas A&M University. Their kind helps contributed to many aspects of this research.

Finally, I would like to thank my parents for their encouragement and patience. It is my luck to have you guys in my life.

CONTRIBUTORS AND FUNDING SOURCES

This work was supported by a dissertation committee consisting of Professor Steven M. Wright, Robert D. Nevels, and Jim Ji of the Department of Electrical and Computer Engineering, and Professor Mary P. McDougall of the Department of Biomedical Engineering.

Contributors and Funding Sources Support from the Texas A&M University Seed Grant program is gratefully acknowledged.

Chapter 2 the final 16-leg birdcage coil and 3D printing piece are mainly designed and fabricated by Travis Carrell from the Biomedical Engineering Department at Texas A&M University, who is a co-worker of this project. The author contributes to the modification and testing of the transmit birdcage's detuning network. Travis also designed and built the custom exercise device, modified the in vivo protocol and helped with the in vivo experiments of the volunteer.

The ^{31}P physiological phantom which simulates the in vivo chemical environment of human skeletal muscle was made by Clayton L. Cruthirds of Center for Translational Research on Aging and Longevity, Department of Health & Kinesiology. He also helped with the in vivo experiments of the volunteer.

All other work described in the dissertation was completed by the author independently.

NOMENCLATURE

NMR	Nuclear Magnetic Resonance
MRS	Magnetic Resonance Spectroscopy
SNR	Signal Noise Ratio
^{31}P	Phosphorus
PCr	Phosphocreatine
ATP	Adenosine-triphosphate
Pi	Inorganic Phosphate
Q_{UL}	Unloaded Quality Factor
Q_L	Loaded Quality Factor
FID	Free Induction Decay
RF	Radio Frequency
B_0	Static Magnetic Field

TABLE OF CONTENTS

Page

ABSTRACT ii

ACKNOWLEDGEMENTS iii

CONTRIBUTORS AND FUNDING SOURCES iv

NOMENCLATURE v

TABLE OF CONTENTS vi

LIST OF FIGURES viii

LIST OF TABLES x

CHAPTER I INTRODUCTION TO NMR AND MRS 1

1.1 Nuclear magnetization and Bloch equation 3

1.2 Effects of the RF pulse 5

1.3 Phenomenological T_1 T_2 Relaxation 8

1.4 System Hardware 9

1.5 RF coil receive sensitivity and transmitter efficiency 10

1.6 MRS pulse sequence 11

References 15

CHAPTER II TRASMIT-ONLY COIL 17

2.1 Saddle Coil 17

2.2 RF shield 21

2.3 Interface circuits 24

2.4 Concepts of Birdcage Coil 28

2.5 Simulations and Experiments of Birdcage Coil 32

References 38

CHAPTER III RECEIVE-ONLY COIL ARRAY 40
3.1 NMR Receiver Coil 40
3.2 Quadrature Mode Receiver Coil 43
3.3 NMR Receiver Phase Array Coil 43
3.4 Design of Four Element Receive-Only Phase Array Coil 47
References 53
CHAPTER IV EXPERIMENTS OF PHOSPHOROUS MRS 55
4.1 1T ONI Magnet and B0 Field Homogeneity 55
4.2 Spectrometer and Pulse Sequence Parameters 59
4.3 Array Signal Processing 61
4.4 85% Phosphoric Acid Phantom ^{31}P MRS 63
4.5 Physiological Concentration ^{31}P Phantom MRS 66
4.6 In-Vivo 31P MRS 68
4.7 The Benefit of Increasing Array Elements 71
4.8 ^{31}P MRS Time Domain Quantification 75
References 82
CHAPTER V CONCLUSION AND FUTURE WORK 84
References 86
APPENDIX A MATLAB CODE FOR ARRAY SIGNAL PROCESSING 87
APPENDIX B VITA 92

LIST OF FIGURES

Page

Figure 1 Procession of Magnetic Moment 4

Figure 2 RF Excitation 6

Figure 3 Free Induction Decay 9

Figure 4 System Hardware 10

Figure 5 Hard Pulse 12

Figure 6 Calf Muscle ^{31}P MRS 13

Figure 7 Saddle Coil 18

Figure 8 Model of Saddle Coil 20

Figure 9 Simulation of Shielded Saddle Coil 22

Figure 10 Coaxial Shield Choke Balun 26

Figure 11 LC Balun 27

Figure 12 Birdcage Coil and Equivalent Circuits 29

Figure 13 Simulation of Birdcage Coil 33

Figure 14 Photo of a 12-leg Birdcage Coil 35

Figure 15 Detuning Network of Birdcage Coil 37

Figure 16 Simulation of Loop Coil 41

Figure 17 Simulation of Figure 8 Coil 42

Figure 18 Circuits of LNA decoupling 45

Figure 19 Circuits of Capacitive Decoupling 46

Figure 20 Receiver Coil Array Diagram 48

Figure 21 Photo of Receiver Coil Array 51

Figure 22 1T Magnet 56

Figure 23 Static Magnetic Field Map 58

Figure 24 Broadband NMR Spectrometer 61

Figure 25 Central Peak Shifting 61

Figure 26 Phosphoric Acid ^{31}P MRS 65

Figure 27 Physiological Concentration ^{31}P Phantom MRS 67

Figure 28 In Vivo ^{31}P MRS 70

Figure 29 Linewidth and SNR Simulation 73

Figure 30 Simulated MRS Quantification 79

Figure 31 In Vivo MRS Quantification 80

LIST OF TABLES

Page

Table 1 Simulated Result of saddle coil and Probe Measurement 24

Table 2 S21 Probe Measurement of Different Transmitter Coils 36

Table 3 Quality Factor of Different Receiver Coils 50

Table 4 Coil Performance of Phosphoric Acid Phantom 65

Table 5 Coil Performance of Physiological Concentration ^{31}P Phantom 68

Table 6 Input Simulated Sine Waves 78

Table 7 LPSVD result of Simulated Sine Waves 78

Table 8 LPSVD result of In Vivo Data 80

CHAPTER I

INTRODUCTION TO NMR AND MRS

Nuclear magnetic resonance (NMR) is a physical phenomenon in which nuclei which have different quantum energy state levels caused by a relatively strong static magnetic field are perturbed by a time-varying magnetic field and respond by producing an electromagnetic signal with the frequency characteristic of the local magnetic field around that nucleus. More specifically, the static magnetic field is generated by strong magnetic sources (ferromagnet, super-conducting coils) applied to the nuclei, the local chemical environment and isotope involved forms the local magnetic field.

Nuclear magnetic resonance spectroscopy (MRS) is a spectroscopic technique uses the NMR phenomenon to measure the local magnetic field around the nuclei, by which the identification of molecular, structure, dynamics, reaction state, and chemical environment are observed. Any nuclei that contain an odd number of protons and neutrons have an intrinsic nuclear magnetic moment can be used in MRS. ^{1}H, ^{13}C, ^{31}P are the most common one being used, other elements like ^{2}H, ^{6}Li, ^{14}N, ^{15}N, ^{19}F, etc. are studied as well, and they all have different unique research purpose in various areas.

In this research, we focus on the ^{31}P human in vivo MRS. ^{31}P MRS offers a unique non-invasive access to investigate the in vivo metabolism and is a significant advancement in the understanding and treating of many disease processes[1][2]. Quantification of the phosphocreatine (PCr), inorganic phosphate (Pi), Adenosine triphosphate (ATP) in ^{31}P MRS directly reflects the human bioenergetics[3][4]. The interest of human in vivo ^{31}P MRS includes skeletal muscle bioenergetics, neuromuscular disorder, cerebral phosphorylated metabolites, coronary heart

disease and metabolic characteristics in tumors, etc [4] . In many of these studies, high temporal resolution ^{31}P MRS are required to monitor the metabolic response to the dynamic exercise in humans [9]. Studies using this technology have reported an increase in the resting inorganic phosphate (Pi) to phosphocreatine (PCr) ratio (Pi/PCr), increases in Pi concentration and reductions in pH, can be measured using ^{31}P MRS.

The challenge of in vivo dynamic ^{31}P MRS mainly originates from the relatively low concentration of human phosphorus and the high requirement of static magnetic field's homogeneity. Hence, conventional dynamic ^{31}P MRS is now almost exclusively done in high field 1.5T/3Tand ultra-high field 7T whole-body MRI system.

Unfortunately, these devices are costly, limiting ^{31}P studies to medical centers. Those factors create practical difficulties in achieving clinic ^{31}P MRS diagnosis and research. The study of dynamic^{31}P MRS to understand muscle energetics, if widely available, could be a useful monitoring tool. Therefore, we investigate the potential for using low-field MRI scanners as a platform to enable low-cost ^{31}P studies outside the conventional hospital environment. Extremity NMR scanners which usually have low (<0.5T) or medium (0.5-1T) field strength are low cost and available research or clinic diagnosis instrument. They are gaining increasing popularity and are very useful to image upper and lower extremities[10]. However, they are seldom used to conduct spectroscopy due to their low intrinsic SNR and lower B_0 homogeneity (as needed for imaging).

Those limitations make high temporal resolution dynamic ^{31}P MRS difficult using conventional NMR signal acquisition technology with low field extremity NMR scanners. To solve these problems, here we propose using a transmit-only volume coil and multi-channel

receive-only array to overcome these limitations. Specifically, we investigated the potential for non-localized dynamic ^{31}P spectroscopy of the human skeletal muscle at a 1 Tesla extremity magnet (ONI Orth-one, Wilmington, MA).

1.1 Nuclear magnetization and Bloch equation

When a sample is placed inside a magnetic field (B_0), a small static nuclear magnetization arises from a small portion of the nuclear moment aligned with the direction of the static field. And from the Boltzmann statistics in the equilibrium state, a total magnetic moment of [11][12]:

$$\mathrm{M} = \frac{N\gamma\hbar^2\omega}{4kT_s} (1.1)$$

The N is the number of the nucleus, γ is gyromagnetic ratio which varies from the different nucleus, $\hbar$ is reduced Planck constant, $\omega = \gamma B_0$ is the angular Larmor frequency, k is Boltzmann's constant and Ts is the sample temperature. This indicates the bulk magnetization is proportional to B_0 field. Once the magnetization is formed, and it's a rather small magnetic moment. under the influence of the B_0, the torque acting on it is

$$\vec{\tau} = \overrightarrow{\mathrm{M}} \times \overrightarrow{\mathrm{B_0}} (1.2)$$

The change of nucleus angular momentum is therefore

$$\vec{\tau} = \frac{\mathrm{d}\vec{\mathrm{J}}}{\mathrm{dt}} (1.3)$$

The gyromagnetic ratio links the nucleus' angular momentum to its magnetic moment by

$$\overrightarrow{M} = \gamma\vec{\mathrm{J}} (1.4)$$

So eventually combine those equations, and we get

$$\frac{d\vec{M}}{dt} = \gamma\left(\vec{M} \times \vec{B_0}\right) (1.5)$$

The solution of this equation assumed with a constant initial magnetic torque of $\vec{M(0)} = M_{x0}\vec{x} + M_{y0}\vec{y} + M_{z0}\vec{z}$ gives

$$\vec{M(t)} = \left(M_{x0}\cos\omega t + M_{y0}\sin\omega t\right)\vec{x} + \left(M_{y0}cos\omega t - M_{x0}\sin\omega t\right)\vec{y} + M_{z0}\vec{z} (1.6)$$

This means the magnetic toque processes about the z-axis which is the direction B0 static field is applied to in the clockwise direction. The result is shown in Fig. 1, the frequency of the precession is called Lamour frequency.

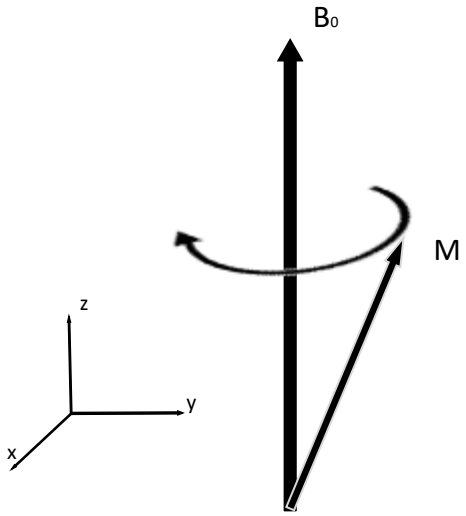

Fig. 1 The nuclear magnetic moment process about the B0 field.

For different types of the nucleus, the Lamour frequency is also different. ^{1}H has Lamour frequency of 42.58 MHz, and ^{31}P has Lamour frequency of 17.24 MHz

1.2 Effects of the RF pulse

We first consider the rotation frame

$$\vec{x}' = \cos \omega_r t \, \vec{x} - \sin \omega_r t \, \vec{y} (1.7)$$

$$\vec{y}' = \sin \omega_r t \, \vec{x} + \cos \omega_r t \, \vec{y} (1.8)$$

Where ω_r is the angular frequency of the frame. And the magnetization in this frame becomes

$$\vec{M} = M_x' \vec{x}' + M_y' \vec{y}' + M_z' \vec{z}' (1.9)$$

When a sine Rf pulse $B_1 = B_{10} \cos \omega t \vec{x}$ is sent into the sample. In the rotating frame, the continuous sine can be decomposed into a clock-wise (CW) and counter-clockwise (CCW) circular polarization wave.

$$\overrightarrow{B_{cw}} = \frac{1}{2} B_{10} (\cos \omega_r t \, \vec{x} - \sin \omega_r t \, \vec{y}) = \frac{1}{2} B_{10} \vec{x}' (1.10)$$

The CCW doesn't have an effect on the magnetization, which means for a linear polarized sine wave only half of its amplitude contribute to the magnetization tip angle. Let's now consider the effect of Bcw.In the rotation frame, the effective B_1 is

$$\overrightarrow{B_{eff}} = \left(B_0 - \frac{\omega_r}{\gamma} \right) \vec{z} + \frac{B_{10}}{2} \vec{x}' (1.11)$$

If the $\omega_r = \gamma B_0$, the rotation frame (or RF sine pulse frequency) has the same frequency as the Lamour frequency (given by the static magnetic field), then this is simplified to

$$\overrightarrow{B_{eff}} = \frac{B_{10}}{2} \vec{x}' (1.12)$$

The magnetization will precess about the B_{eff} (x-axis in this case) in the rotation frame. The rotation angular frequency is

$$\omega_{rot} = \gamma |B_{eff}| (1.13)$$

T duration sine pulse is applied, the tip angle is

$$\theta = \gamma |B_{eff}| T (1.14)$$

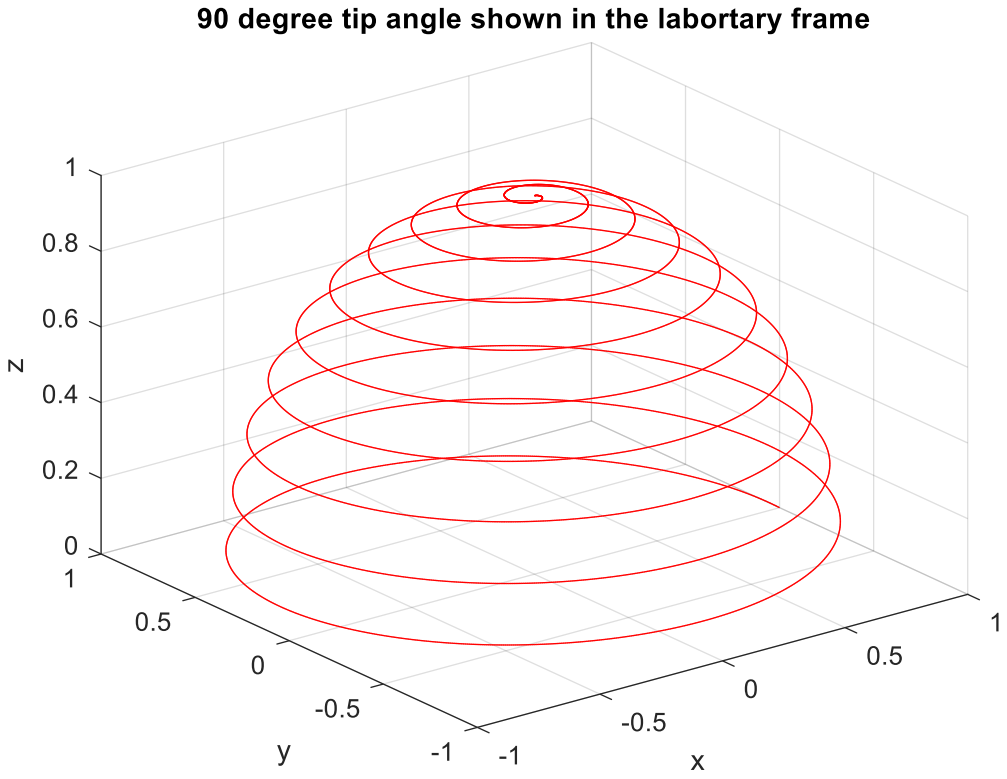

Fig. 2 The magnetization is tipped by the rf pulse of exact Lamour frequency, a pulse duration of 10 times the precession period is assumed in here.

Now let's consider the situation that RF sine pulse is slightly off resonance $\omega_r \approx \gamma B_0$.

$$\overrightarrow{B_{eff}} = (B_0 - \frac{\omega_r}{\gamma})\vec{z}' + B_1\vec{x}' = \frac{\Delta\omega_0}{\gamma}\vec{z}' + B_1\vec{x}' (1.15)$$

This suggests that effective field has two components: the usual B_1 component pointing along the x'-axis and a residual component $\frac{\Delta\omega_0}{\gamma}$ along z' axis. We would predict a precession of M about the B_{eff}, and the analysis can be obtained by directly solving the following Bloch equation,

$$\frac{dM_x}{dt} = \Delta\omega_0 M_y' (1.16)$$

$$\frac{dM_y}{dt} = -\Delta\omega_0 M'_x + yB_1 M'_z (1.17)$$

$$\frac{dM'_z}{dt} = -\gamma B_1 M'_y (1.18)$$

The closed-form solution doesn't exist for an arbitrary envelope of B_1. If we send a hard pulse $B_1 \prod\left(\frac{t-\Gamma_P/2}{\Gamma_P}\right)$, the magnetization components along each axis immediately after the pulse are given by,

$$M'_x = M_z^0 \sin\theta\cos\theta(1-\cos\alpha)(1.19)$$

$$M'_y = M_z^0 \sin\theta\sin\alpha(1.20)$$

$$M'_z = M_z^0(\cos^2\theta + \sin^2\theta\cos\alpha)(1.21)$$

$\omega_{eff} = \sqrt{\Delta\omega_{0+}^2 \omega_{rot}^2}$ and $\theta = \arctan\left(\frac{\omega_{rot}}{\Delta\omega_0}\right)$

The transverse magnetization immediately after the pulse is no longer along the y-axis as in the case of on-resonance excitation but has a phase shift φ_0 from the y-axis toward the x-axis, which is given by

$$\tan\varphi_0 = \frac{Mx}{My} = \tan\frac{\alpha}{2}\frac{\Delta\omega_0}{\omega_{eff}}(1.22)$$

$\alpha = \omega_{eff}\Gamma_p$ is now the flip angle about the axis of the effective magnetic field. It's evident that the phase shift φ_0 increases almost linearly with the frequency shift $\Delta\omega_0$, it would cause a first-order phase shift in the MRS and can be problematic. In addition, the magnitude of the transverse magnetization decreases as the frequency offset increases.

1.3 Phenomenological T1 T2 Relaxation

After the RF is sent into the sample, the Mx, My transverse component of the magnetization

starts to decay or dephase due to the nuclear spin-spin interaction or spin energy exchanges. Bloch used an exponential decay with constant T_2 to phenomenologically model this complex quantum mechanism.

In the meantime, the net magnetization M returns to its initial maximum M_0 parallel to B_0 due to spin-lattice relaxation which means the nuclear spin is perturbed by the nearby proton or electron. This is also model by another phenomenologically exponential growth function with constant T_1. Combining the T_2 transverse relaxation of the M_{xy}, and the longitudinal T_1 relaxation of M_z. we finally get the Bloch equation

$$\frac{dM_{x,y}}{dt} = \gamma\left(\overline{M} \times \vec{B}\right)_{x,y} - \frac{M_{x,y}}{T_2} (1.23)$$

$$\frac{dM_z}{dt} = \gamma\left(\overrightarrow{M} \times \vec{B}\right)_z + \frac{M_0 - M_z}{T_1} (1.24)$$

Assume the initial magnetization of $M_z(0) = M_0\vec{x}$, which means a 90-degree tip angle, and solve this equation we have

$$M_x(t) = M_0 \exp\left(\frac{-t}{T_2}\right)\cos(\gamma B_0 t) (1.25)$$

$$M_y(t) = -M_0 \exp\left(\frac{-t}{T_2}\right)\sin(\gamma B_0 t) (1.26)$$

$$M_z(t) = M_0\left[1 - \exp\left(\frac{-t}{T_1}\right)\right] (1.27)$$

The transverse M_{xy} can be detected by the coil and signal shown as a so-called free induction decay (FID). Take the Fourier transform of this time domain signal, a resonance peak in the

spectral domain shows up, and it's the simplest form of MRS which only has one frequency component.

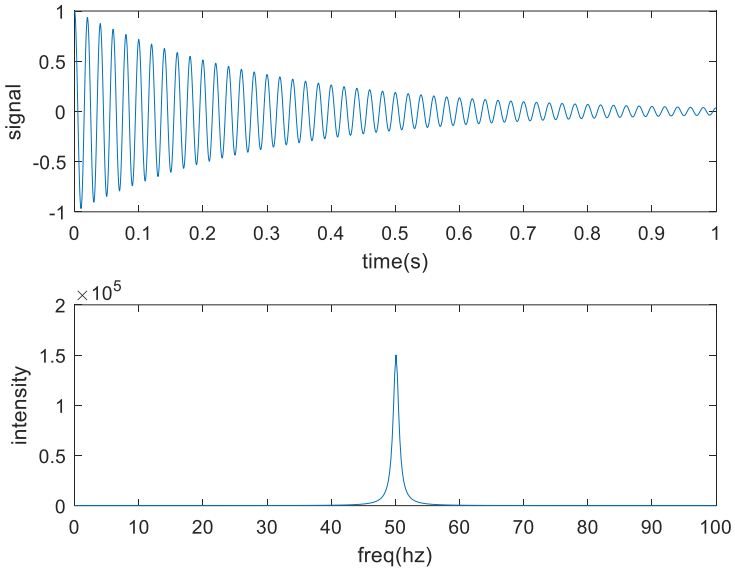

Fig. 3 The FID of a 50hz Lamour frequency induction with a T_2=300ms decay and corresponding real part of the spectra.

1.4 System Hardware

When the magnetization starts to process about the z-axis on the x y plane, a coil which is sensitive to B_{xy} can be placed on the sample to detect the signal generated by EM faraday induction, typically μV level. It is then connected to a low noise preamplifier (LNA)to amplify the signal to detectable mV level and sampled by ADC. Sine hard pulse generated by DAC is used as Rf excitation pulse, typically amplified by a power amplifier (PA) to about 100W for a 90-degree tip angle. Besides for the main magnet, multiple channels B0 shim coils are also used to improve the local B0 magnetic field homogeneity.

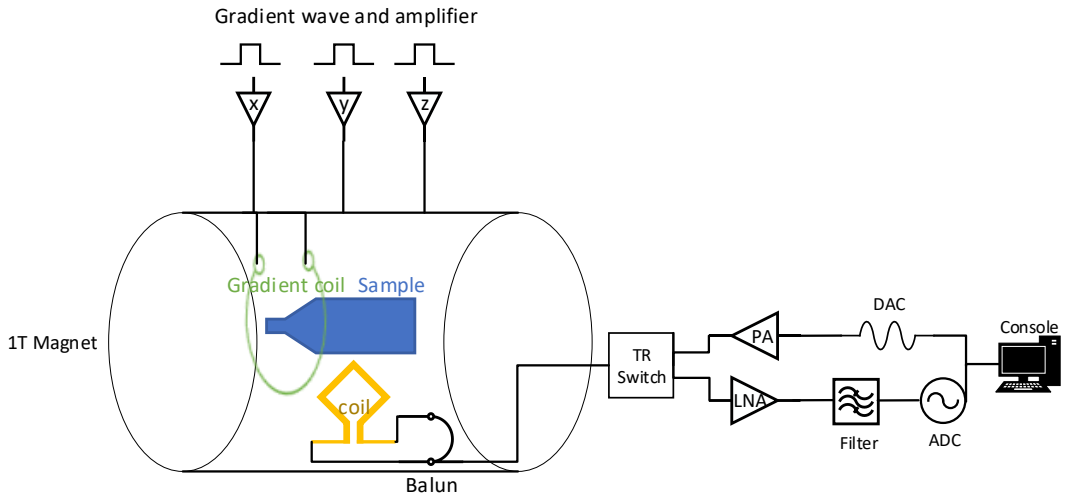

Fig.4 The brief diagram of MRS hardware.

1.5 RF coil receive sensitivity and transmitter efficiency

Among all the hardware for doing NMR experiment, Rf coils are directly related to the signal and noise ratio (SNR) of the received signal. By using the Reciprocity theorem, the RF antenna detects the induced voltage given by [12]

$$\xi = \iiint_{Sample} \frac{\partial}{\partial t}(\overrightarrow{B_1} \cdot \vec{M}) dv (1.28)$$

The $\overrightarrow{B_1}$ is the hypothetical field at a magnetic moment due to unit loop current.

The thermal noise voltage density is

$$\sqrt{4kTR} (1.29)$$

$R=R_c+R_L$, R_c is the coil resistance, and R_L is the sample loss.,

And the R_c of a cylindrical wire considered the skin effect can be predicted by

$$Rc = L/p\sqrt{\mu\omega_0\rho/2} (1.30)$$

L is the length of the wire conductor, p is the circumference of the wire, and ρ is the resistivity.

Load resistance is originated from the conductive loss of the phantom, which is affected by the phantom conductivity and coil electrical field distribution.

Considering a specific region of interest (ROI), The signal and noise ratio (SNR) is[13]

$$\frac{\omega_0 M|B_1|}{\sqrt{4KTR\Delta f}}(1.31)$$

The B_1 is the effective magnetic field created by 1 amp current. The SNR of the whole volume is

$$K\eta M(\mu_0 Q\omega_0 v_c / 4kT\Delta f)^{1/2}(1.32)$$

$Q=\frac{\omega L}{R}$ is the quality factor of the coil,K is a constant related to coil geometry, and η is the filling factor.

In the transmit mode, Transmit Power dissipation can be calculated by $P=0.5I^2R$, and B∼I. There is a duality relationship between the coil used as a transmit mode and receive mode.

1.6 MRS pulse sequence

There are three major types of MRS pulse. The simplest one is the non-localized hard pulse, which is a continuous sinusoid pulse that has a specific time duration. It has been theoretically discussed in section 1.2. The bandwidth of hard pulse is defined as $\frac{1}{4T}$, T is the pulse duration. Typically, the pulse duration is less than 1000us to ensure all the magnetization is equally excited within the bandwidth of interest. After a short time duration (100 μs-2ms), the received signal is sampled for an acquisition time window 128ms-1000ms. The hard pulse is a non-localized, which means the signal will be received from all the volume's magnetization excited

by the RF pulse. The pros of this is maximum signal intensity is received. On the other hand, all the noise from the sample volume is received as well. The hard pulse will be the pulse sequence we mainly use in this study since in low field NMR, because the highest possible signal is desired and noise is mainly dominated by coil itself rather than sample noise.

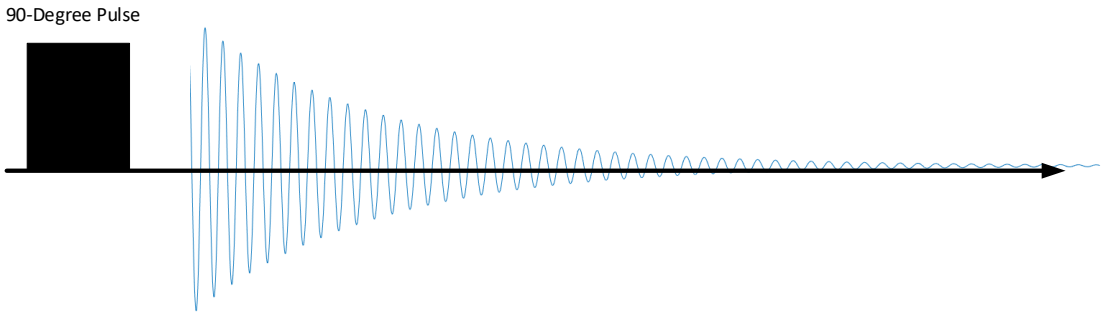

Fig. 5 Hard pulse diagram.

Time domain signal wavelet is sampled, one can apply various methods to retrieve the information from it. The most common method is applying Fast Fourier Transform to obtain the spectral domain MRS. Usually, on the x-axis, people show the spectrum from positive value to the negative value in the unit of parts per million (ppm).

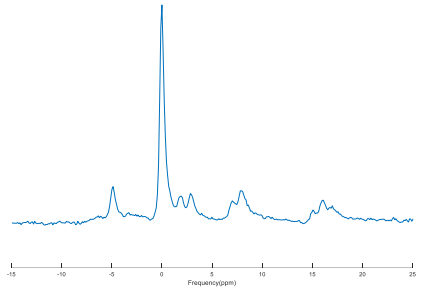

(a)

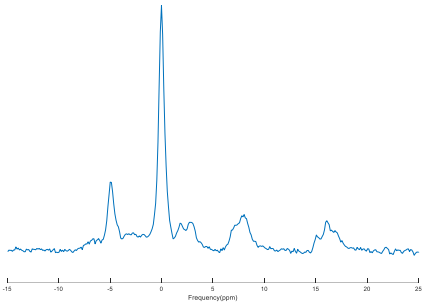

(b)

Fig. 6 ^{31}P in vivo calf muscle MRS taken with a volunteer during rest and exercise.

Single voxel spectroscopy (SVS) use sequentially applied RF pulses and gradients to localize the signal received from a small cubic region of interest. There are many different techniques to implement the SVS sequence. For example, image-selected in vivo spectroscopy (ISIS), which is the most popular type of single-voxel sequence used in ^{31}P MRS. Because the frequency information must be saved in spectroscopy, Frequency coding cannot be used in MRS. ISIS uses the x y z gradients' slice intersection for voxel localization. right separate RF & Gradient pulse cycle are applied in order and then added and subtracted to obtain the final defined voxel of

interest. Each selective 180 pulse and corresponding gradient invert the amplitude of magnetization along one dimension [14].

Another type of multi-voxel MRS is called chemical shift imaging (CSI) [15]. It utilizes phase-encoding for spatial localization. It can work from one to three dimension. The phase encoding is applied to modulate only the signal's phase and amplitude before the signal acquisition. Thus, the spatial chemical shift information, which is sampled during the next acquisition window, will not be distorted by the temporal modulation of phase encoding. The data reconstruction is, therefore, straightforward using Fourier transformations. The disadvantage of CSI is, because phase-encoding is applied in all spatial dimensions, the whole process becomes very time-consuming.

The reason we choose non-localized MRS in this project is we want to obtain the highest signal possible from the sample and avoid long acquisition time.

References

[1] Hu, M. T. M., Taylor-Robinson, S. D., Chaudhuri, K. R., Bell, J. D., Labbe, C., Cunningham, V. J., ... & Brooks, D. J. (2000). Cortical dysfunction in non-demented Parkinson's disease patients: A combined 31P-MRS and 18FDG-PET study. Brain, 123(2), 340-352.

[2] Minshew, N. J., Goldstein, G., Dombrowski, S. M., Panchalingam, K., & Pettegrew, J. W. (1993). A preliminary 31P MRS study of autism: evidence for undersynthesis and increased degradation of brain membranes. Biological psychiatry, 33(11-12), 762-773.

[3] Kemp, G. J., &Radda, G. K. (1994). Quantitative interpretation of bioenergetic data from 31P and 1H magnetic resonance spectroscopic studies of skeletal muscle: an analytical review. Magnetic resonance quarterly, 10(1), 43-63. W.-K. Chen, Linear Networks and Systems. Belmont, CA: Wadsworth, 1993, pp. 123–135.

[4] Arnold, D. L., Matthews, P. M., &Radda, G. K. (1984). Metabolic recovery after exercise and the assessment of mitochondrial function in vivo in human skeletal muscle using 31P NMR. Magnetic resonance in medicine, 1(3), 307-315.

[5] Argov, Z., & Bank, W. J. (1991). Phosphorus magnetic resonance spectroscopy (31P MRS) in neuromuscular disorders. Annals of Neurology: Official Journal of the American Neurological Association and the Child Neurology Society, 30(1), 90-97.

[6] Barbiroli, B., Montagna, P., Cortelli, P., Funicello, R., Iotti, S., Monari, L., ... & Lugaresi, E. (1992). Abnormal brain and muscle energy metabolism shown by 31P magnetic resonance spectroscopy in patients affected by migraine with aura. Neurology, 42(6), 1209-1209.

[7] Yabe, T., Mitsunami, K., Inubushi, T., & Kinoshita, M. (1995). Quantitative measurements

of cardiac phosphorus metabolites in coronary artery disease by 31P magnetic resonance spectroscopy. Circulation, 92(1), 15-23.

[8] Negendank, W. (1992). Studies of human tumors by MRS: a review. NMR in Biomedicine, 5(5), 303-324.

[9] Davies, R. C., Eston, R. G., Fulford, J., Rowlands, A. V., & Jones, A. M. (2011). Muscle damage alters the metabolic response to dynamic exercise in humans: a 31P-MRS study. American Journal of Physiology-Heart and Circulatory Physiology.

[10] S. Ghazinoor, J. V. Crues, and C. Crowley, "Low-field musculoskeletal MRI," Journal of Magnetic Resonance Imaging, no. 25, pp. 234-244, 2007.

[11] Liang, Z. P., & Lauterbur, P. C. (2000). Principles of magnetic resonance imaging: a signal processing perspective. SPIE Optical Engineering Press.

[12] Jin, J. (1998). Electromagnetic analysis and design in magnetic resonance imaging (Vol. 1). CRC press.

[13] Hoult, D. I., & Richards, R. E. (1976). The signal-to-noise ratio of the nuclear magnetic resonance experiment. Journal of Magnetic Resonance (1969), 24(1), 71-85.

[14] Ordidge, R. J., Connelly, A., & Lohman, J. A. (1986). Image-selected in vivo spectroscopy (ISIS). A new technique for spatially selective NMR spectroscopy. Journal of Magnetic Resonance (1969), 66(2), 283-294.

[15] Skoch, A., Jiru, F., &Bunke, J. (2008). Spectroscopic imaging: basic principles. European journal of radiology, 67(2), 230-239.

CHAPTER II

TRANSMIT-ONLY COIL

Magnetic resonance spectroscopy or imaging can be conducted using one single coil as transmit and receive mode. It is well known that transmit volume coil like birdcage or saddle coil can produce very uniform B_1 pattern and tip angle over a large space, which can ensure all the spins in ROI to be tipped approximately 90 degrees. But their B_1 sensitivity is very low because the noise from all the sample will be detected when used as a receive coil, and resistance of the coil itself is also very high. Since the power efficiency usually is not the constraint of the NMR experiment, but the received SNR is, the volume coil is usually used as a transmit-only coil in MRS/MRI.

In this chapter, we discuss two types of transmit coil designs and their pros and cons. We also use pin diode and high speed-pin diode driver to implement transmit-only control of the coil [1]. We first designed a linear mode ^{31}P saddle coil resonating at 17.24MHz. But the power efficiency of it is not high enough to achieve a 90-degree tip angle within 500us pulse duration using a 500W commercial power amplifier. To improve this coil power efficiency issue, our current design is a transmit-only low-pass quadrature mode birdcage [2].

2.1 Saddle Coil

The most conventional type of volume coil is a saddle coil. Saddle coil is formed by two rectangle loops curved on a cylinder. The angle of the curved arc is typically 120 degree. Distributed capacitors C_b usually are added to break the coil every 1/20 λ to ensure uniform current distribution. The current distribution on these two rectangle loops generates a B_1 field

pattern similar to Helmholtz pair so that the B_1 pattern is very homogeneous in the central region of the saddle coil. One saddle coil can only generate linear mode By field. Thus, it is 3db less efficient than quadrature mode coils we will introduce later. Since the resonance frequency of ^{31}P at 1T is 17.24MHz, which is at a very low field. The transmitter power consumption is mostly dominated by the coil, shield or interface circuits rather than sample. This has been confirmed by measuring the Q_L/Q_{UL} of the saddle coil which is found to be very close to 1.

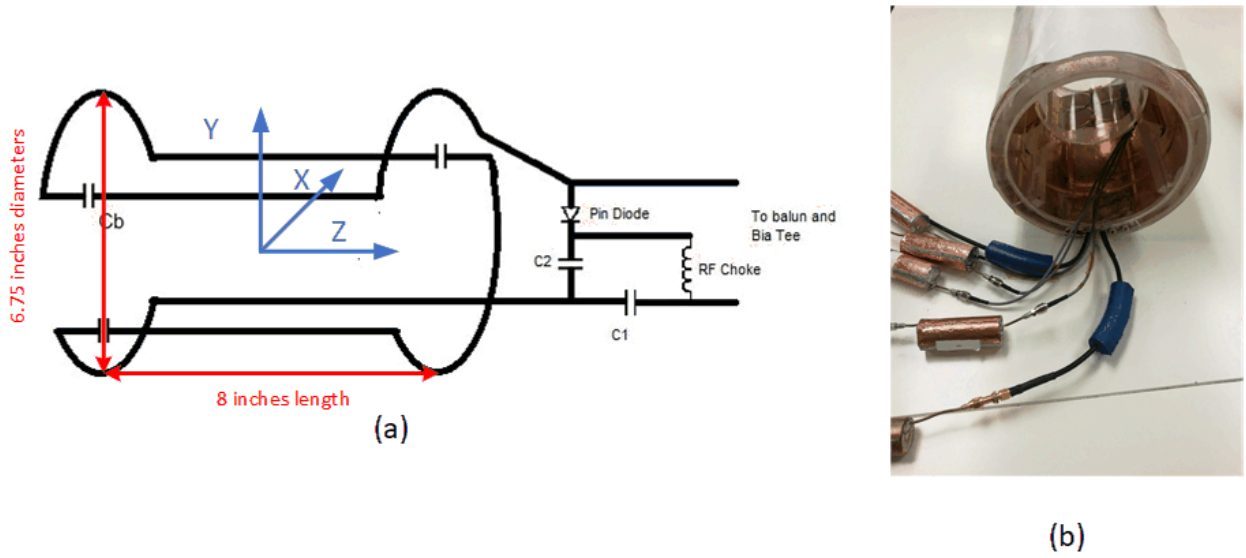

Fig. 7 (a) Diagram of the transmit-only saddle coil. (b) The saddle the author designed and built is 203.2 mm long and 171.45mm diameter. Shield diameter is 203.2mm .The saddle is curved on the inner PVC cylinder, and RF shield made by 4 oz copper with intersection capacitors break the shield into 4 pieces to prevent eddy current from the gradient. Balun is connected to the coils as well.

The saddle coil can be modeled as one inductor plus the resistance from the copper strip, and sample. The C_2 is used to cancel the inductance so that it resonates at 17.24MHz. The pin diode series with the C_2 will be reversed bias during the receiving window and forwards bias during the transmitting window controlled by the gate signal duration. The RF signal and DC gate signal are combined by the bias tee and then fed to the matching network. The RF choke is added between the pin diode to let the DC gate signal pass through. Using this method, the coil can be detuned by the DC gate signal during the receiving window so that the transmitting noise leakage will be prevented from the receiving and receive coil will not couple to the transmitter coil.

The simulation result of a saddle coil without shield using Remcom XFDTD is shown in Fig. 8 to obtain the B_1 field pattern and B_1/amp. Due to the factor that coil resistance is determined by various fabrication difference like the material used, capacitors loss, soldering joint loss, etc. It's complicated to incorporate all those factors into simulation and give a very accurate result matches the reality. Thus, the purpose of simulation here is only to predict the B_1 pattern and study the effect of RF shield, and coil dimension to transmit efficency. An accurate prediction of the total coil transmitting efficiency and pulse duration achieved from 500W input is done with 90-degree pulse calibration of the saddle coil from MRS experiments. And later the actuate transmitting efficiency of the birdcage coil is predicted by the S21 probe measurement of relative value.

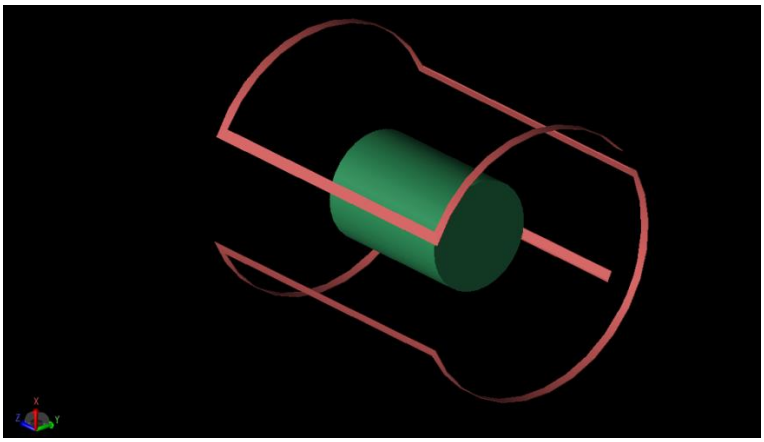

(a)

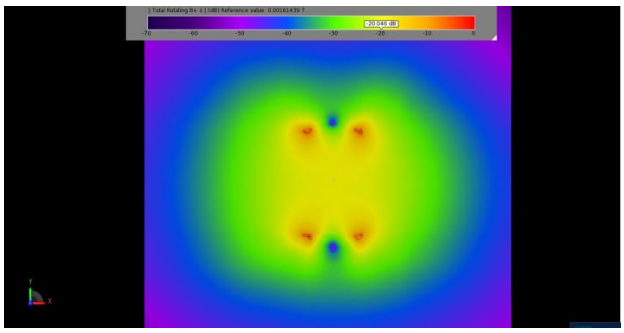

(b)

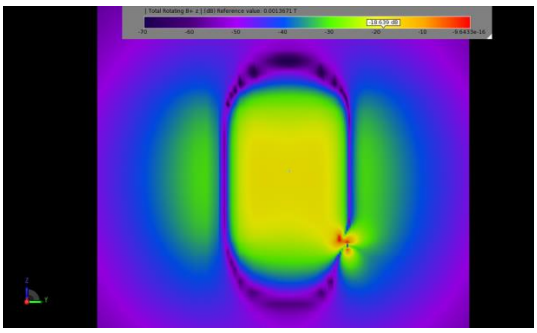

(c)

Fig.8 (a) Simulated physical model of an unshielded saddle coil. The phantom is a 9.6cm long and 3.5cm radius. The conductivity of the phantom is 1s/m, and the relative dielectric constant is 80 which emulates the electrical properties of the saline[3]. (b) shows the simulated $|B_1^+|$field patterns of the central axial, and (c) sagittal slices.

The input impedance is found to be 0.1699+139.774j. When input power is 100w, there is 34.307A current on the port. The $|B_1^+|$of the central region is about 1.6059e-04Tesla and maintained to be within a 60mm radius circle, which can be considered homogeneous enough for the region of interest (ROI) we care in this project. We also observe the RF field seems to be not

perturbed by the saline phantom, which is expected at low frequency since less conductivity current and displacement current are less.

2.2 RF shield

The RF shield is in general necessary to be put outside the transmitter coil to prevent the RF pulse from leaking into the magnet and eliminate the possible coupling between the coil and gradients. It ensures the stability of the coil tuning. To entirely block the RF shield, the RF shield needs to be at least 4 times thicker than the skin depth(15.7μm) of 17.24MHz frequency. So, we choose to use 4oz, 139.2μm thickness copper sheet to build the shield. On the other hand, when the RF shield is placed very close to the coil, the mirror current will flow on the RF shield, and it will cancel the RF field generated by the coil so that the transmitting efficiency is significantly reduced. In this project, due to the constraint of the magnet bore size and the space for fitting the leg inside. The RF shield has to be close to the transmitting coil itself. The diameter of the shield used here is 203.2mm which is a 15.875mm distance to the saddle coil. Here we use Remcom FDTD EM simulation to model the effect of the shield to the B_1^+ field.

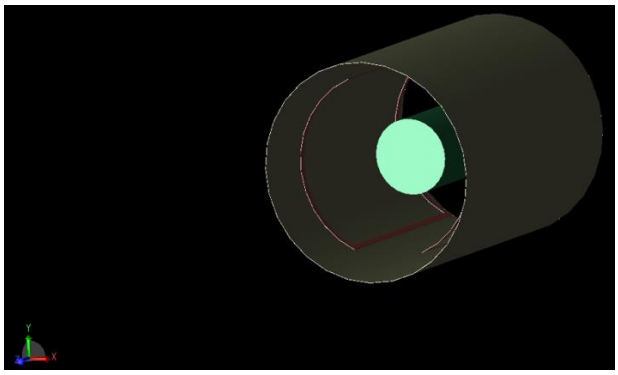

(a)

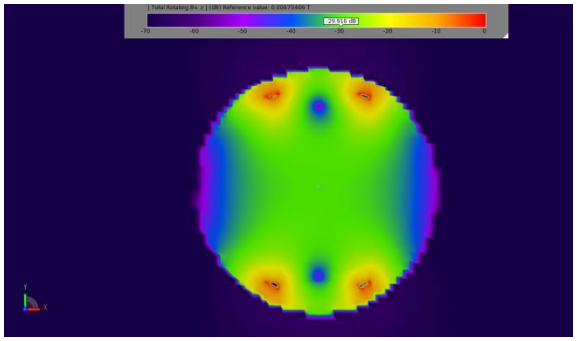

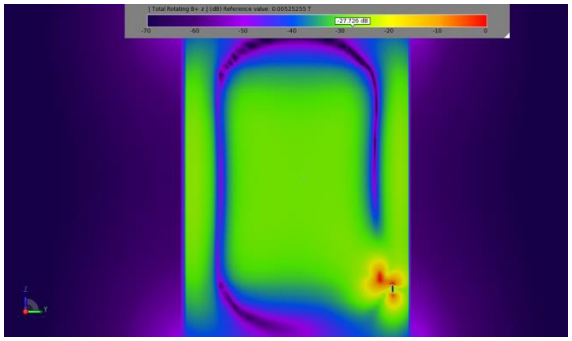

(b) (c)

Fig.9 (a) The physical model of saddle coil with shield, (b) simulated $|B_1^+|$ field patterns of the central axial, and (c) sagittal slices.

When input power is 100w, the input impedance is found to be 0.01123+89.682j, and 133.443A current on the port. The shield degrades the inductance of the saddle coil so that the imaginary input impedance decreases. The $|B_1^+|$ of the central region is about 2.1566e-04Telsa. Apparently, near the shield's boundary, the RF is perturbed/canceled by the shield's mirror current. But the central ROI homogeneity of the B_1 field still meets our requirement of this project. In this situation result, 4.584% of the power is radiated, and 95.416% of the power is dissipated in the phantom. So, we can conclude the shield works well to block the RF field.

The shielded saddle coil's $|B_1^+|$/Unit Current (Telsa/A) is 2.89 times worse than the unshielded case. This indicates the shield will largely reduce the effective magnetic field.

It is worth to mention here, these simulation results assume perfect electrical conductivity of coil's strip and ideal capacitors, and all the loss is either from radiation or phantom's conductivity. At 17.24MHz frequency, our experiments result both from transmitting coil or receiving coil both confirm that main loss is actually coil's resistance or other hardware' ohm and insertion loss, which is not taken into account in the FDTD simulation. Those losses are from various sources, such as copper strip ohm loss, soldering joints loss, capacitors/inductors loss, etc., and practically measured from Vector Network Analyzer (VNA).Thus, we don't apply these simulation results to directly predict the power required to achieve the desired magnetization tip angle. Nevertheless, we can quantify the $|B_1^+|$/Unit Current and use this value to interpret the effects of the shield to B_1^+ field.

For the bench measurement, we placed a B_1 probe at the center in the saddle coil, orthogonal to the field direct so that maximum signal can be coupled to the probe and measure the S21 (Port 1 saddle coil, Port 2 probe) with or without the shield, and during both measurement the saddle coil S11 are retuned to 50ohm. It can be shown the S21 measurement value using the same probe is directly proportional to the coils' efficiency ($|B_1^+|$/Unit Current/$\sqrt{R}$) [4]. The imaginary part of the input impedance from the simulation result and S11 measurement are different because the distributed capacitors are added to the real saddle coil but not on the simulation.

Table 1 $|B_1^+|$/Unit Current of Shield/Unshielded saddle coil and Probe S21 Measurement.

	Simulated $\|B_1^+\|$/Unit Current (Telsa/A)	Simulated Input impedance(ohm)	Probe S21 measurement (db)	S11 Input impedance measurement (ohm)
Unshielded	4.6810e-06	0.1699+139.774j	-37.7	2.16+77.94j
Shield	1.6161e-06	0.01123+89.682j	-46.1	1.67+27j

We can see from table 1 that unshielded simulated B_1/Unit Current is 9.2db higher than shielded, and S21 probe measurement is 8.4db higher. The shielded saddle coil has a less real part of the input impedance, probably due to less radiation loss.

Another significant thing to be considered for the shield is eddy current due to the gradient. In the MRI or CSI, rapid gradient pulses are used to do frequency/phase coding. Those gradient pulses mainly have acoustic range frequency, and they need to penetrate the shield, which means the RF shield needs to be transparent to the gradient pulse so that no eddy current will flow on the shield. To achieve this, the RF shield needs to be segmented and use break-up capacitors to connect the gaps between different segments. The segmented RF shield emulates a high-pass filter.

2.3 Interface circuits

The matching network is usually not perfectly balanced, which means the asymmetric structure of the matching network will allow common mode signal between signal and ground sides. This would create issues when a coaxial cable is attached after the unbalanced matching

network. Part of the current will flow on the outer shield of the coaxial cable. This part of the current will radiate, create additional loss and noise, and affect the matching of the coil. The balun is a 3-port device that connected between coil's matching networks and coaxial cable to cancel the common mode signal and stop the current from flowing on the outer surface of the coaxial cable. There are different types of balun such as sleeve balun, coaxial shield choke balun, LC balun and transformer-like balun[5]. Here we investigate coaxial shield choke balun and LC balun which is the most commonly used types of the balun in RF coil.

Coaxial shield choke balun prevents the current from flowing on the surface of the coaxial cable. To make such balun, first we need to cover the coaxial cable's shield with dielectric tape and wire it to make an inductance by the shield, then insert the whole cable into a dielectric cylinder and cover it with another additional shield. Solder the additional shield to the coaxial cable's shield on the side which is close to the next stage preamplifier, and adds a capacitor to connect the additional shield and coaxial cable's shield on the other side which is close to the coil. After tuning the parallel capacitor's value to resonate the LC tank at the desired frequency with the inductor made by coaxial cable's outer shield, the outer surface current is choked so that the common mode signal will be rejected.

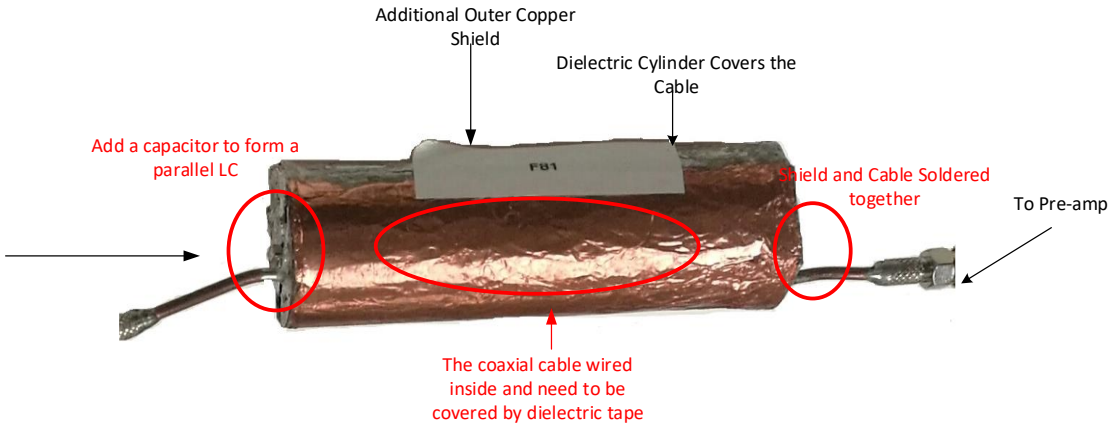

Fig.10 The picture of a coaxial shield choke balun.

LC balun [6] is a three-port that transfer unbalanced port to balanced ports. Two pairs of anti-symmetric LC phase shifter are used to shift one balance ports. The inductors' and capacitors' value is chosen based on the balanced (R_S) and unbalanced ports' (R_L) impedance.

$$\mathrm{X} = \sqrt{R_S R_L} (2.1)$$

$$\mathrm{L} = \frac{X}{2\pi f_0} (2.2)$$

$$\mathrm{C} = \frac{1}{X 2\pi f_0} (2.3)$$

This makes the LC balun's performance sensitive to the load impedance. If the impedance from the coil's end is changed and becomes different from the designed value, the amplitude and phase of two differential ports will not be equal and 180 out of phase anymore, which not only degrade the common mode rejection performance but also decrease the differential signal. Since the NMR coils' impedance may be sensitive to the load (patients), and SNR is the most critical optimization goal of this project, I chose not to use LC balun in the end.

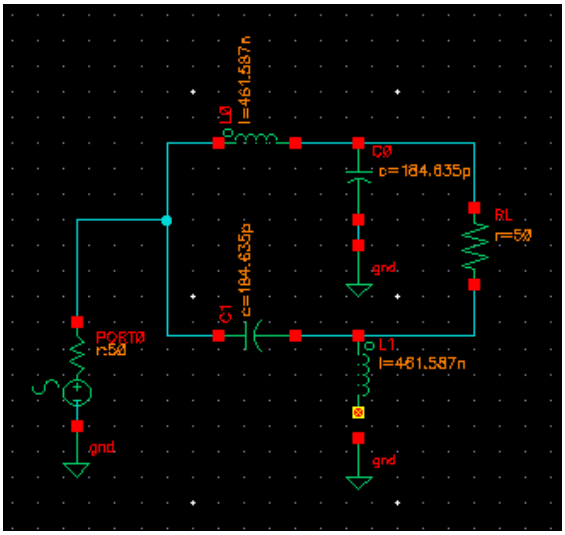

Fig.11 the circuits' diagram of LC balun designed at 17.24MHz with balanced / unbalanced sides' impedance both 50 Ohms.

Bench test of the balun is made by soldering a SMA connector on the LC circuits and measuring S11 of this SMA port. If the LC circuits of the balun is tuned well, the S11 measurement of this port should show rejection mode. Usually S11 of the resonance should be at least -20 db lower than baseline. Notice this method is only actuarate when the frequency of interest is low. This because the additional phase of the SMA and parasitic capacitor will add measurement error at high frequency.

The coaxial shield choke balun is chosen in the end, because it is not sensitive to the impedance mismatch of the coil, and the cable loss is small at this low frequency. Two coaxial shield chokes were made for the transmit coil, and four for the receiver array, below -20db isolation is measured from the current injection method.

2.4 Concepts of Birdcage Coil

The birdcage coil is made of several equally spaced vertical strips on a cylindrical surface, whose ends are connected by horizontal strips. Conventionally, people call the vertical strips "leg" and horizontal strips "end ring". If the distributed capacitors are only placed on the end rings, it's called high-pass birdcage. If the distributed capacitors are only placed on the middle of the legs, it is called low-pass birdcage. If the distributed capacitors are placed both on end rings and legs, it's called hybrid birdcage.

Birdcage coil is designed to discrete 0-360 degree current phase distribution on each leg, and thus delivers homogeneous linear magnetic field in the center of the coil. Next, we introduce the theory of the birdcage coil to illustrate how it works and how to design birdcage based on eigenmode analysis [7]

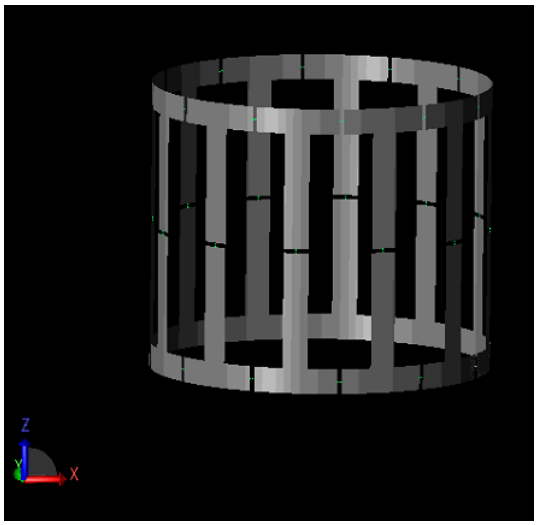

(a)

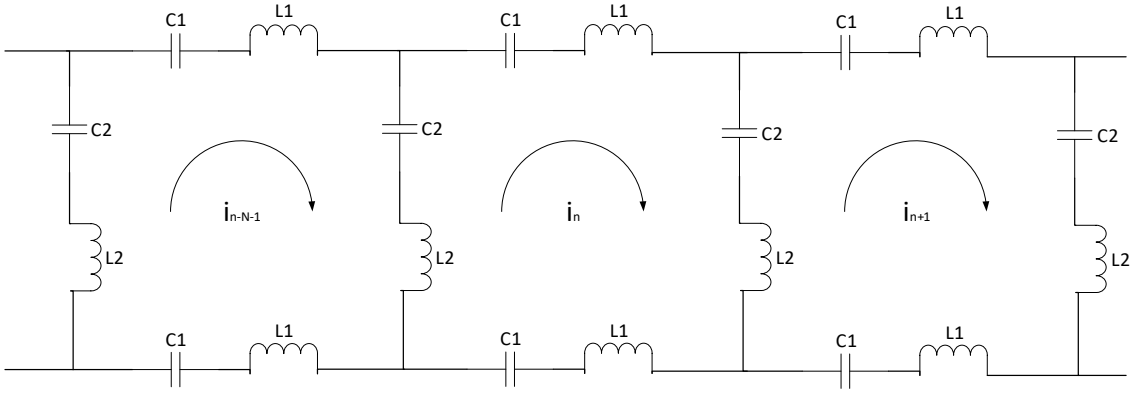

(b)

Fig.12 (a) The diagram of 12-leg hybrid birdcage. (b) the equivalent circuits of the hybrid birdcage coil (general case, where capacitors are both on legs and end rings) neglecting the mutual inductance.

Assume the number of legs of the birdcage coil is equal to N, apply KCL to each cell of the equivalent circuits, and define $M_0 = L_1 + L_2$ as total self-inductance,$M_m$as mutual inductance between different cells, $s = j\omega$, the equations can be formulated as

$$\sum_{m=0}^{N-1} I_{n+m} M_m + 2I_n \left(\frac{1}{C1} + \frac{1}{C2}\right) - \frac{1}{C2}(I_{n+1} + I_{n+N-1}) = 0 \quad (2.4)$$

$$n=0 \text{ to } N \quad (2.5)$$

These equations can be represented by the circulant matrix

$$M = \begin{pmatrix} M_0 & M_1 & \cdots & M_{N-1} \\ M_{N-1} & M_0 & \cdots & M_{N-2} \\ \vdots & \vdots & \ddots & \vdots \\ M_1 & M_2 & \cdots & M_0 \end{pmatrix}, \quad (2.6)$$

$$E = \begin{pmatrix} -2(\frac{1}{C1} + \frac{1}{C2}) & \frac{1}{C2} & 0 & \cdots & \frac{1}{C2} \\ \frac{1}{C2} & -2(\frac{1}{C1} + \frac{1}{C2}) & \frac{1}{C2} & \cdots & 0 \\ \vdots & \vdots & \vdots & \ddots & \vdots \\ \frac{1}{C2} & 0 & \frac{1}{C2} & \cdots & -2(\frac{1}{C1} + \frac{1}{C2}) \end{pmatrix}, \quad (2.7)$$

$$I = \begin{pmatrix} I_0 \\ I_1 \\ \vdots \\ I_{N-1} \end{pmatrix}, \quad (2.8)$$

$$EI = S^2 MI. \quad (2.9)$$

The eigendecomposition of the last equation is

$$\tilde{\mathrm{E}}\tilde{\mathrm{I}} = \mathrm{S}^2\tilde{\mathrm{M}}\tilde{\mathrm{I}},(2.10)$$

$\tilde{\mathrm{E}}$,$\tilde{\mathrm{M}}$ are the diagonal eigenvalue matrix. The kth term of them are

$$\tilde{\mathrm{E}}_k=-2[\frac{1}{C1}+\frac{1}{C2}(1-cos\frac{2\pi k}{N})],(2.11)$$

$$\tilde{\mathrm{M}}_k=\sum_{m=0}^{N-1} M_m \exp(-j2\pi km/N).(2.12)$$

$\tilde{\mathrm{I}}$ is the eigenvectors of the N-point DFT,$\tilde{\mathrm{I}}_k = i_0\exp(-j2\pi km/N)$, which represents the complex current value of the mth cell at the kth resonance mode. The resonance mode frequency is

$$\mathrm{f} = \frac{1}{2\pi}\sqrt{\frac{\tilde{\mathrm{E}}}{\tilde{\mathrm{M}}}} = \frac{1}{2\pi}\sqrt{\frac{2}{\tilde{\mathrm{M}}_k}[\frac{1}{C1}+\frac{1}{C2}(1-cos\frac{2\pi k}{N})]}.(2.13)$$

Because $\mathrm{M_m}=\mathrm{M_{N-m}}$, it results in N/2-1 degenerate resonance mode. The current flow on the kth leg of the birdcage is

$$I_k = \tilde{\mathrm{I}}_k - \tilde{\mathrm{I}}_{k-1} = -2i_0\sin\frac{\pi m}{N}\mathrm{j}\exp(\frac{-j2\pi m(k-1/2)}{N}).(2.14)$$

When m=0, there is no current flows on the legs. Thus, this mode is called the end-ring mode. When m=1, the current amplitude is uniform on each leg and has 2π/N phase shift to the adjacent legs. This means the current's phase change periodically on the birdcage, and a very uniform linear $\mathrm{B_1}$ pattern will be created inside the birdcage coil.

The value of self-inductance $\mathrm{L_1}$, $\mathrm{L_2}$, and mutual inductance M_m could be computed by inductance calculation handbook [8]. The capacitors $\mathrm{C_1}$ and $\mathrm{C_2}$ could be obtained based on the inductance value by plugging to resonance mode frequency equation [9]. Ref. [10] offer software package to do inductance calculation and eigenmode analysis for birdcage.

Birdcage coil could be driven in quadrature mode by feeding two ports with 90-degree phase shift on orthogonal legs of the coil. This will ideally create a circular polarization magnetic field, which is mathematically formulated by $B_1^+ = B_x\vec{x} + B_y j\vec{y}$. As stated in the chapter one 1.2, quadrature mode circular polarization is 3db more efficient than the linear mode operation.

2.5 Simulations and Experiments of Birdcage Coil

The choice of different types of birdcage coils depends on the operating frequency and practical capacitor value available. At 17.24MHz, 317.2pf capacitors can be utilized to implement a 12-leg 120mm long, 140.6 mm diameter, trace width 12.7 mm low pass birdcage. Other types of birdcage coil may require an impractical value of capacitors thus not chosen to be utilized here.

The motivation of replacing the saddle to birdcage coil as the transmitter is, we found out the shielded saddle coil requires a 1000us pulse to obtain a 90-degree tip angle using a 500W maxima output of the broadband power amplifier available in the lab. This pulse duration equal to 250Hz bandwidth which is too narrow for ^{31}P MRS. We want to shorten the pulse duration below 500us without using higher input power. The birdcage coil due to its quadrature mode operation, will give us 3db more efficiency.

We first investigate the FDTD simulation of a 120mm long, 171.45 mm diameter low-pass birdcage coil with a 203.2mm long shield. The FDTD model and result are shown in Fig. 13. We can observe from (b) (c) that when port 1 is excited, By field maintains to be very homogeneous inside the birdcage and obtain $|B_1^+|$ =1.7675e-06Telsa/A in the center. Similarly, from (d) (e), when port 2 is excited, Bx field maintains to be very homogeneous as well and obtain $|B_1^+|$

=1.8765e-06Telsa/A.(f) shows the quadrature mode circular $|B_1^+|$field achieving by feeding on two orthogonal ports simultaneously with 90-degree phase shift, $\frac{|B_1^+|}{Ports\ Average\ Current}$ =3.3546e-06Telsa/A. (g) shows the $|B_1^-|$anti-quadrature mode.

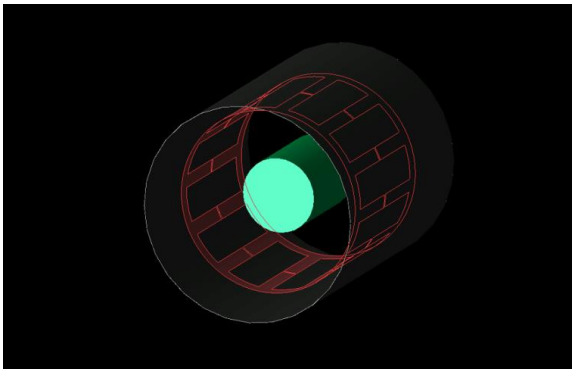

(a)

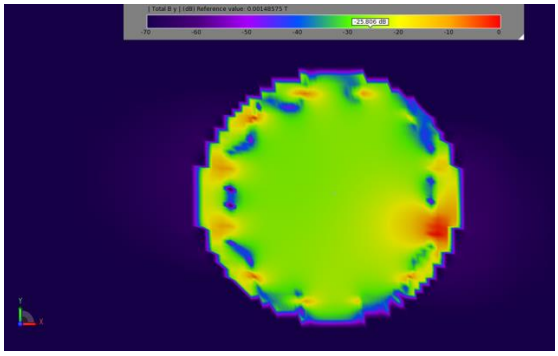

(b)

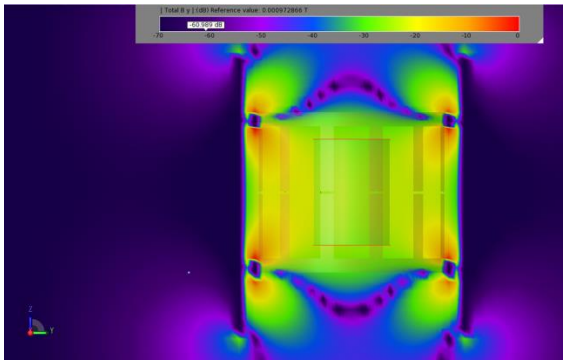

(c)

Fig. 13 (a) The model of birdcage coil with shield (b) simulated axial By field of feeding on port 1(c) simulated sagittal By field of feeding on port 1 (d) simulated axial Bx field of feeding on port 2 (e) simulated sagittal Bx field of feeding on port 2 (f) shows the axial quadrature mode $|B_1^+|$field (feeding on port 1 and port 2 with 90-degree phase shift) (g) shows the axial quadrature mode $|B_1^-|$ field (feeding on port 1 and port 2 with -90-degree phase shift).

Fig. 13 Continued

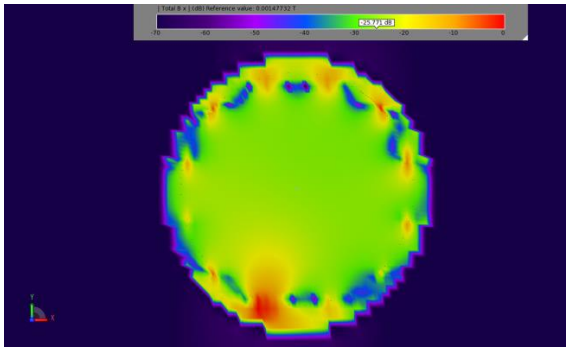

(d)

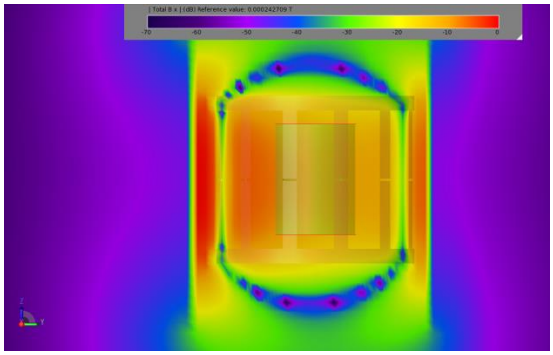

(e)

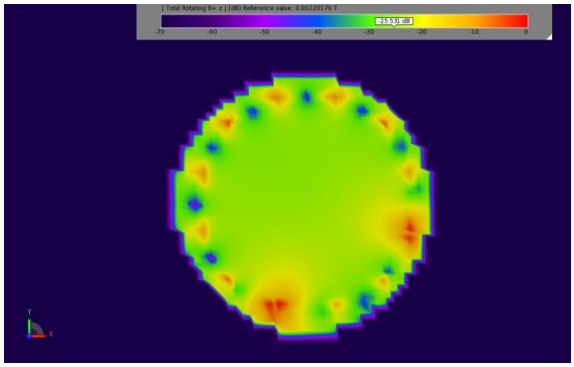

(f)

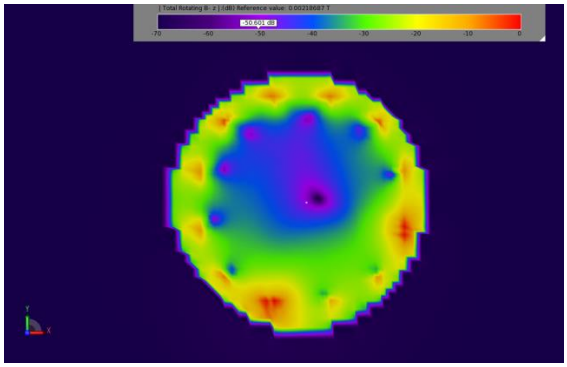

(g)

It is found from the simulation that the birdcage's B_1^+ field is significantly reduced by the shield. To increase the transmission efficiency, the author decided to change the dimension to 120mm long and 140.6mm diameter so that the shield can have less effect on the birdcage coil.

The simulation result of port 1 linear excitation is 1.0910e-05 Telsa/A in the geometric center of the birdcage coil. And Quadrature mode operation obtains 1.5252e-05 Telsa/A. Thus, about 6.17 times better B_1/amp efficiency is obtained by using a smaller diameter birdcage which mitigates the effect of mirror current.

A 12-leg birdcage of the dimension mention above was then fabricated , and we compared the transmit efficiency of it to the saddle coil built. The Fig. 14 shows the birdcage and modes observed from the LNA.

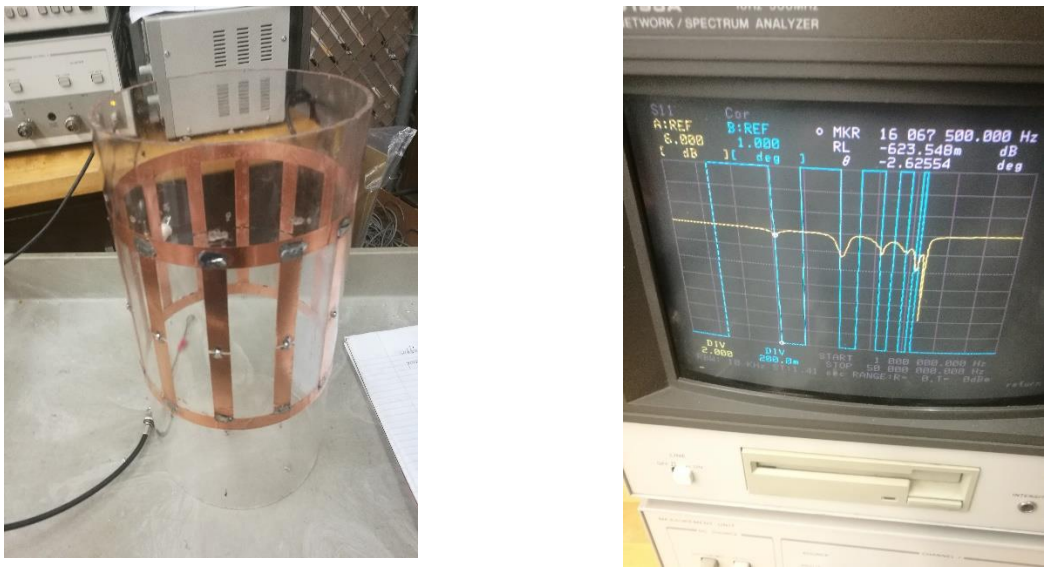

(a) *(b)*

Fig.14 12-leg birdcage and its resonance modes are shown in the LNA.

Table 2 shows experimental S21 probe measurement comparisons of linear mode birdcage coil and saddle coil with or without the shield. We can see from the S21 probe measurement that the shielded linear birdcage is 10.2db more efficient than the shielded saddle coil. If taking into account the additional 3db from the quadrature mode, we can predict the pulse duration will be shortened from 1000us to 218.7us using the same input power.

The quadrature operation will require additional quadrature combiner to split the power and add the 90-degree phase shift. The implement of such circuits can be found in microwave lecture. We build a quadrature combiner operated at 17.24MHz using lumped elements and find it has about 0.6db insertion loss, which is relatively small.

Table 2 S21 Probe Measurement of Different Transmitter Coils

	S21 probe measurement (db)
Unshielded saddle coil (171.45 OD)	-43.4
Shielded saddle coil (171.45 OD)	-51.8
Unshielded linear birdcage (140.7 OD)	-35.1
Shielded linear birdcage (140.7 OD)	-41.6

To meet the magnet's spatial constraints and volunteer's comforts, our final design is a 16-leg 165mm long 178mm diameter low pass birdcage with 216mm diameter shield. It is utilized for the phantom and volunteer test. The 90-degree pulse duration calibrated with full concentration ^{31}P is found to be 300us which corresponds to 833.3Hz or 48.4ppm for ^{31}P. This successfully meets the bandwidth requirement of ^{31}P MRS. This birdcage coil also has active detuning circuits on the two input ports implemented by pin diode and bias control circuits as shown in Fig.15.

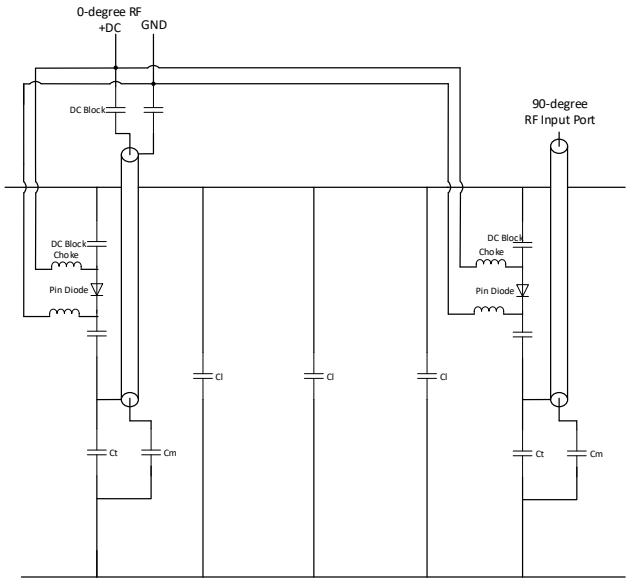

Fig. 15 Simplified circuits diagram of the transmit-only birdcage.

References

[1] Barberi, E. A., Gati, J. S., Rutt, B. K., & Menon, R. S. (2000). A transmit‐only/receive‐only (TORO) RF system for high‐field MRI/MRS applications. Magnetic Resonance in Medicine: An Official Journal of the International Society for Magnetic Resonance in Medicine, 43(2), 284-289.

[2] Hayes, C. E., Edelstein, W. A., Schenck, J. F., Mueller, O. M., &Eash, M. (1985). An efficient, highly homogeneous radiofrequency coil for whole-body NMR imaging at 1.5 T. Journal of Magnetic Resonance (1969), 63(3), 622-628.

[3] Haynes, W. M. (2014). CRC handbook of chemistry and physics. CRC press.

[4] Hoult, D. I., & Richards, R. E. (1976). The signal-to-noise ratio of the nuclear magnetic resonance experiment. Journal of Magnetic Resonance (1969), 24(1), 71-85.

[5] T/R Switches, Baluns, and Detuning Elements in MRI RF coils, Xiaoyu Yang, Tsinghua Zheng, and Hiroyuki Fujita.

[6] Harrison, W. H., Arakawa, M., &McCarten, B. M. (1987). U.S. Patent No. 4,682,125. Washington, DC: U.S. Patent and Trademark Office.

[7] Leifer, M. C. (1997). Resonant modes of the birdcage coil. Journal of Magnetic Resonance, 124(1), 51-60. Giovannetti, G. (2014).

[8] Thompson, M. T. (1991). Inductance calculation techniques—approximations and handbook methods. Power Control Intelligent Motion.

[9] Birdcage coils: Equivalent capacitance and equivalent inductance. Concepts in Magnetic Resonance Part B: Magnetic Resonance Engineering, 44(2), 32-38.

[10] Chin, C. L., Collins, C. M., Li, S., Dardzinski, B. J., & Smith, M. B. (2002). BirdcageBuilder: design of specified‐geometry birdcage coils with desired current pattern

and resonant frequency. Concepts in Magnetic Resonance: An Educational Journal, 15(2), 156-163.

CHAPTER III

RECEIVE-ONLY COIL ARRAY

3.1 NMR Receiver Coil

NMR receiver coil is used to receive the Faraday induction signal of the rotating magnetization. Although, ideally all the transmitter coil introduced in chapter Ⅱ can be used as receiver coil as well. But due to the larger size and RF field coverage of them, the transmitter coil's sensitivity is relatively low during the receiving mode. And it will result in lousy signal and noise ratio (SNR). Thus, for the study that has a high requirement of SNR such as ^{31}P MRS, it is necessary to separate transmitter coils and receiver coils to ensure both uniform magnetization tip angle and highest receiver sensitivity. [1] Various type of surface coils are commonly used as a receiver coil because they only produce highly sensitive B_1 field near the coil and has much less ohm loss compared with volume coil. We introduce here two types of surface coil that are used in this project.

Loop coil is probably the most common type of surface coil. It generates a B_1 field mostly perpendicular to the surface plane and decays fast with distance away from the coil. At a distance approximately less than the radius of the loop, the B_1 field is relatively homogeneous. Fig. 16 shows a 4.5cm-diameter one turn loop coil, with a saline phantom placed 5mm above it, and its $|B_1^-|$ distribution.

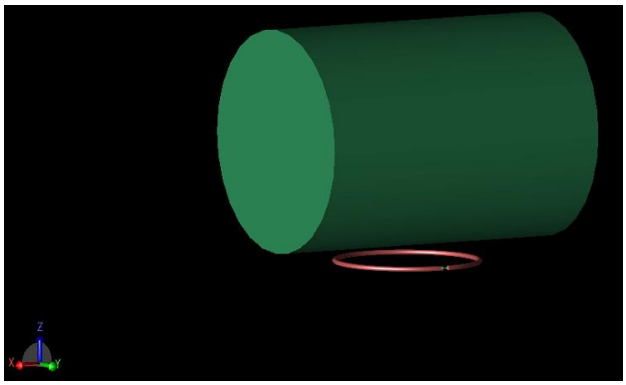

(a)

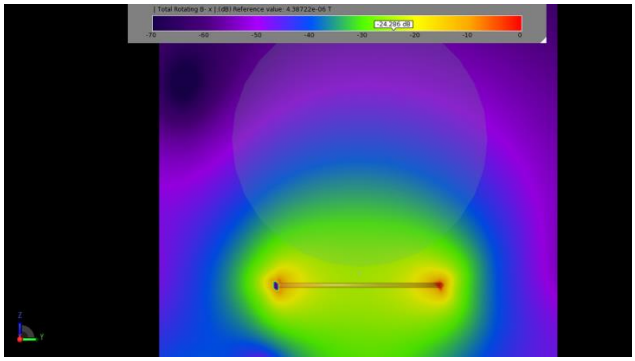

(b)

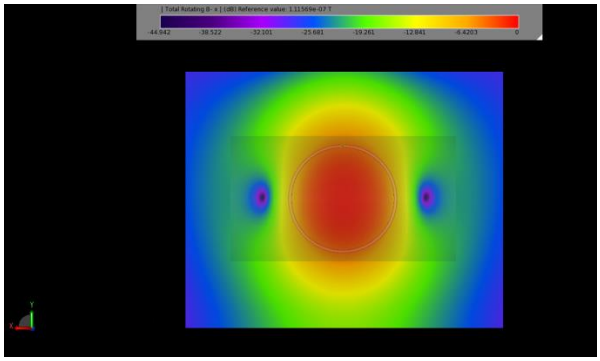

(c)

Fig. 16 (a) Loop coil's physical model. FDTD simulated $|B_1^-|$distribution of (b) axial slice, and (c) coronal slice.

The $|B_1^-|/A$ 1cm above the center of the loop coil is found to be1.3018e-05Telsa/A. This is much higher than the volume coil's as expected.

Figure 8 uses two loops with opposite current direction to form the B_1 field that is mainly horizontal above the center of it. The ohm loss of figure 8 coil is larger than the loop coil and its $|B_1^-|/A$ is less than the loop coil. Thus, its sensitivity is less than the loop coil. Fig.17 shows the

physical model of figure 8 coil with a 45mm diameter of each loop. Other geometry structure can also be used to form figure 8 coil and need to be optimized to give the best B_1^- field. The $|B_1^-|/A$ 1cm above the center of the loop coil is found to be 4.8687e-06Telsa/A.

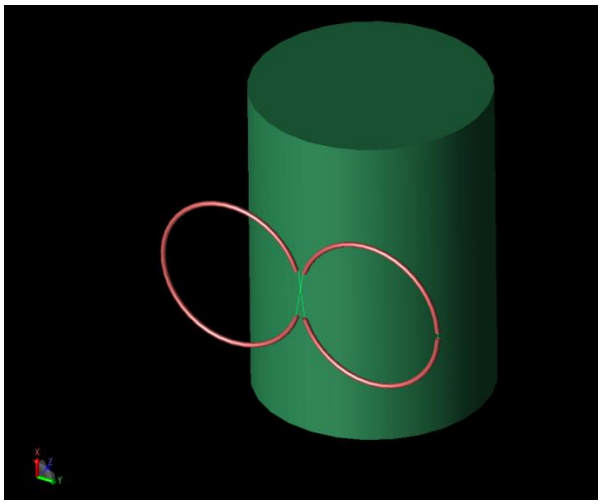

(a)

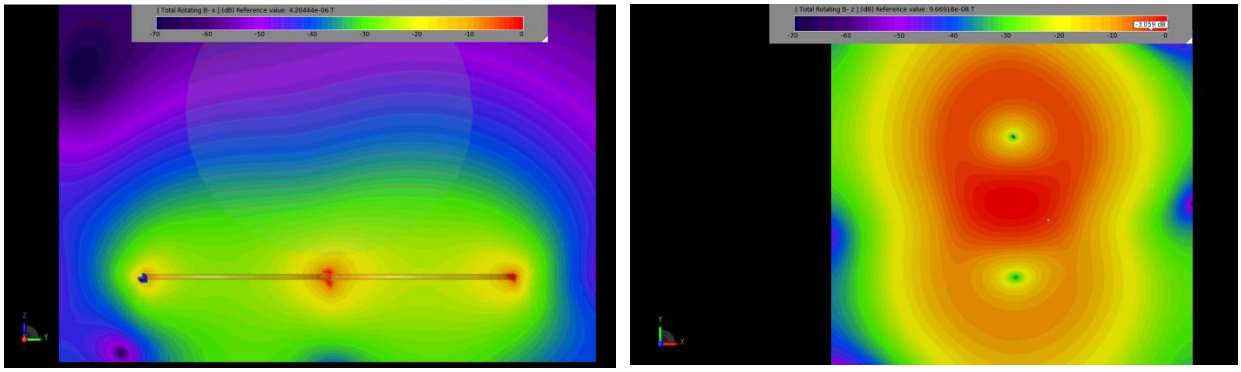

(b) (c)

Fig. 17 Figure 8 coil's physical model, and FDTD simulated $|B_1^-|$ distribution.

There are many other types of the surface coil like D-shape coil, meander coil, etc., which will find their own utilities in specific application seniors [2].

3.2 Quadrature Mode Receiver Coil

In the receiving mode, coils that have quadrature mode circular B_1^- field will ideally have 3db more SNR just like in the transmitting mode. The loop generates mostly B_1 field perpendicular to its surface, and the figure 8 coil generates mostly B_1 field tangential to its surface. One could achieve that by combiner one loop coil with another figure 8 coil. Although perfect 3db more SNR is in general hard to achieve since bother loop coil and figure 8 coil will generate undesired field components, and optimize each coil's B_1 sensitivity to result in an optimal B_1^- field is hard as well. It is worth to mention that the sample noise received from two quadrature coil are uncorrelated since they are from two orthogonal B_1component. [3]

3.3 NMR Receiver Phase Array Coil

NMR phased array was first introduced by Hyde [4] and Roemer [5], it simultaneously acquires multiple channels' signal from non-interacting receive coils array and subsequently combines the data using the proper method. The advent of combing multiple channels signal if the decoupling is done perfectly comes from the factor that different channels' noise is uncorrelated when coil dominated, and are partial correlated if sample dominated [6]. Christopher used a four-element array to obtain better single voxel SNR compared with a single channel for 31P MRS [7]. Wright

theoretically proved that improved sensitivity at all depths could be achieved by replacing a single coil with an array of multiple smaller coils covering the same area [8].

The additional issue arises with the multiple channels' coil is mutual coupling between different channels must be eliminated. When mutual coupling existed between different channels, it will create additional noise received from other channels, causing signal crosstalk and artifact, making the coil input impedance tuning not possible. Thus, how to decoupling coils has been an important research topic.

For conventional loop coil, the mutual coupling between adjacent channels can be eliminated by overlapping the coil by a ¼ diameter of the loop. This method is commonly called geometry decoupling. The theory behind that is simply adding a mutual capacitive coupling to cancel the mutual inductive coupling. For non-adjacent channels, other methods have been used to decouple them, which depends on the type of coils, operating frequency, application seniors. We introduce here two most common methods for decoupling surface coil.

Low input impedance decoupling [5] connects the coil to a low input impedance preamplifier. The designed resonance trap forms a high impedance parallel with the input port of the coil so that no current will flow on the receive coil and no mutual coupling from the B_1 field will happen, but the induced voltage is transferred to the preamplifier and amplifies the signal to the next stage. Fig. 18 shows the circuits diagram of the resonance trap and low input impedance LNA.

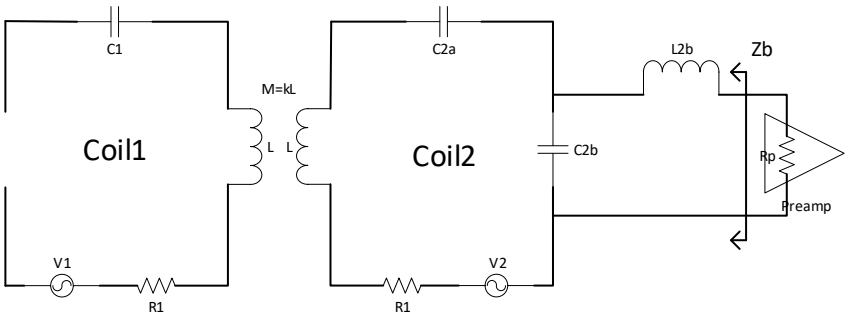

Fig. 18 Circuits diagram of LNA decoupling.

$$Z_b = \frac{{X_{C2b}}^2}{R_1} + j(X_{L2b} - X_{C2b}) (3.1)$$

To obtain a Zb=50ohm impedance match, the C2b and L2b's value can be chosen as

$$X_{L2b} = X_{C2b} = \sqrt{50R1} = X2 (3.2)$$

If the input impedance of preamplifier is close to zero, L2B and C2B form a parallel resonant circuit. The performance of the decoupling relays on how high the impedance can achieve, and thus, depends on how low the input impedance of the preamplifier can be.

The reason why preamplifier decoupling is not utilized here is, practically the input impedance of the preamplifier will have non-zero input impedance [5], and for adjacent coils that have a strong coupling, this will cause a considerable increase in the noise power. Thus, overlapping decoupling is still necessary for decoupling adjacent coils. Secondly, 17.24MHz is not a low impedance LNA commercially available band, custom design and additional cost of the preamplifier is required.

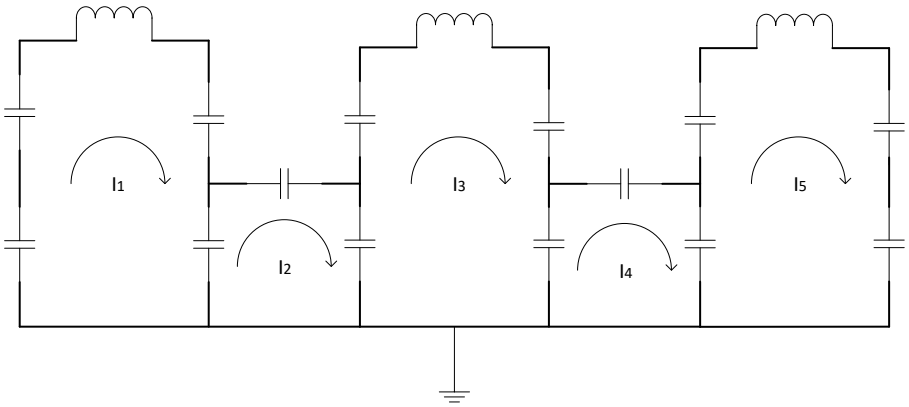

Fig. 19 Circuit diagram of a three-element array using capacitive coupling.

Capacitive/Inductive decoupling [9] use interleaving capacitors/inductors to cancel the mutual coupling between non-adjacent coils. An example of a three-element coil and its analysis is shown in Fig.19. The matrix representation of this circuit can be formulated by,

$$\tilde{Z} = \begin{pmatrix} j\omega L + \sum_{i=1}^{4} \frac{1}{j\omega C_i} & \frac{-1}{j\omega C_4} & j\omega M & 0 & 0 \\ \frac{-1}{j\omega C_4} & \frac{1}{j\omega C_4} + \frac{1}{j\omega C_5} + \frac{1}{j\omega C_7} & \frac{-1}{j\omega C_7} & 0 & 0 \\ j\omega M & \frac{-1}{j\omega C_7} & j\omega L + \sum_{i=6}^{9} \frac{1}{j\omega C_i} & \frac{-1}{j\omega C_9} & j\omega M \\ 0 & 0 & \frac{-1}{j\omega C_9} & \frac{1}{j\omega C_9} + \frac{1}{j\omega C_5} + \frac{1}{j\omega C_4} & \frac{-1}{j\omega C_4} \\ 0 & 0 & j\omega M & \frac{-1}{j\omega C_4} & j\omega L + \sum_{i=1}^{4} \frac{1}{j\omega C_i} \end{pmatrix}$$

(3.3)

$$\tilde{Z}\tilde{I} = 0 \quad (3.4)$$

All the capacitors and mutual/self-inductors' value can be found from bench measurement. The $\tilde{I}$ is a column vector of nontrivial mesh currents. Interleaving capacitor C5 is found by iterating the matrix's eigen value so that all three eigen value align at the same desired resonant frequency.

This method is not used here because the extra space it requires may add difficulties to the shimming procedure.

3.4 Design of Four-Element Receive-Only Phase Array Coil

In this project, we are looking for a design of receiver array that has maxima possible SNR ratio, and also occupies limited space since the SNR of ^{31}P at 1T is relatively low and the bore size of the extremity scanner creates spatial constraints of the receiver array[11]. The capacitive decoupling requires additional space for inserting the interleaving capacitors, and the low impedance preamplifier decoupling results in unavoidable decrease of the SNR. Thus, we design and propose a four-channel quadrature receiver-only phase array coil using two pairs of loop coil and figure 8 coil that is separated by a distance of ¼ diameter (Fig. 20). It takes advantage of the geometry decoupling distance are the same for both loop coil and figure 8 coil to achieve perfect decoupling without using any additional traps, and the overall size is more compact, and SNR performance is better than other conventional design.

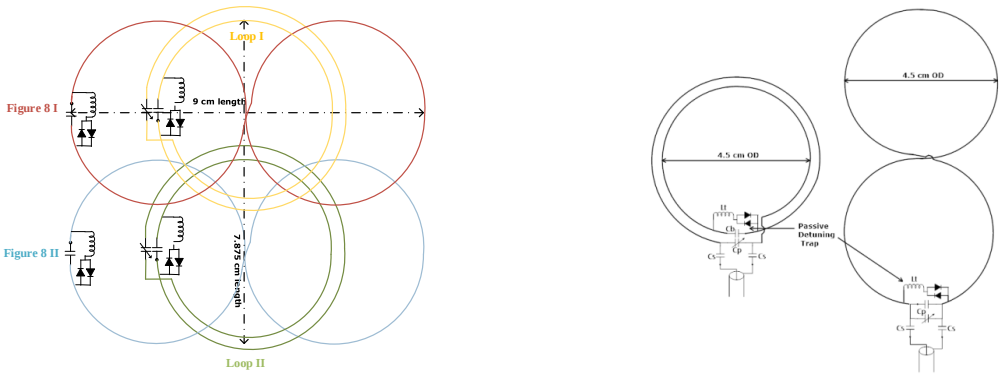

(a) (b)

Fig.20 (a) The whole array configuration. Loop coils are placed at the center of the figure 8 coil. In order to geometry decouple all four channels, two pairs of loop and figure 8 coil are separated by a distance of single coil's ¼ diameter. The final array is curved on a 3D printing and made from AWG 21 copper wire. (b) The single element of the array, the left one is a two turns loop coil, the right one is the figure 8 coil. Passive detuning trap is built with the distributed capacitor Cb and the parallel capacitor Cp. For each channel, solenoid balun is attached. Cs=47pf, Cp=280pf, Cb=820pf, Lt=101nH. For figure 8 coil, Cs=47pf, Cp=330pf, Lt=270nH.

Some of the characteristics of the array are discussed here. Low impedance preamplifiers are not required to decouple the coils in this design. Less than -20db ports isolation is achieved for all four channels. Moreover, one can also use quadrature hybrid combiner to save half of the ADC channels with some additional cost of SNR. Since figure 8 coil and loop coil have orthogonal B_1 field pattern, the noise correlation between them from the sample can be reduced. Lastly, the sensitive region of the coil array is more compact compared with the traditional four-

element loops' design, which helps to keep the array's sensitive region inside the static magnetic field's most homogeneous region.

Lt and Cb form an LC parallel circuit to stop the current from flowing on the coil during transmitting. The back-to-back Schottky diode pairs ensure that the parallel circuits are only active during the transmitting when the transmitting pulse induced voltage on the receiver coil. Thus, the receiver coil is detuned during transmitting and tuned during receiving.

The lamp elements' values are given as follow, for loop array Cs=47pf, Cp=280pf, Cb=820pf, Lt=101nH. For figure 8 coil, Cs=47pf, Cp=330pf, Lt=270nH.

To optimize the SNR performance of each channel. We tested several different design and material of coils.

The coils' diameters are chosen to be 4.5cm. The loaded and unloaded quality factors of different coils are shown in table 3. PPL 1111C/P series high Q, low ESL/ESR non-mag capacitors are used to build the coil. Q_L, Q_{UL} means the loaded and unloaded quality factor of the coils. Physiological concentration 31P phantom (Conductivity 0.9 s/m) is used as loading sample in these measurements.

1.We tested one turn/two turns (one distributed capacitor) for potential increasing of the coil sensitivity and quality fact, all using copper wire and diameter equal to 4.5cm. One distributed capacitor is used on the two turns loop coil for detuning trap.

2.Load and Unload quality fact (Q_L, Q_{UL}) is measured to quantify the sensitivity of different coils. Percentage of the noise source from the sample and coil is measured from Q_L/ Q_{UL}. A large 9cm×8cm loop coil (one distributed capacitor) which is about the same

overall dimension as the arrays are tested as a comparison.

3.One turn coil made with the 1oz copper clad board is built to test the coil material effect to the ohm loss. Another AWG 17 diameter copper wire is used to build a two turns loop coil (with one distributed capacitor) to test if thicker wire diameter can reduce the ohm loss.

Table 3 Quality Factor of Different Receiver Coils

Coil	Q_{UL}	Q_L	Q_L / Q_{UL}
Two turns loop coil (one distributed capacitors)	182	158	0.87
Figure 8 coil	159	151	0.95
One turn loop coil	156	141	0.90
9cm×8cm large loop (one distributed capacitors)	200	115	0.58
One turn loop coil made with 1oz copper	96	90	0.94
2 turns loop coil made with AWG 21 wire (one distributed capacitors)	197	154	0.78

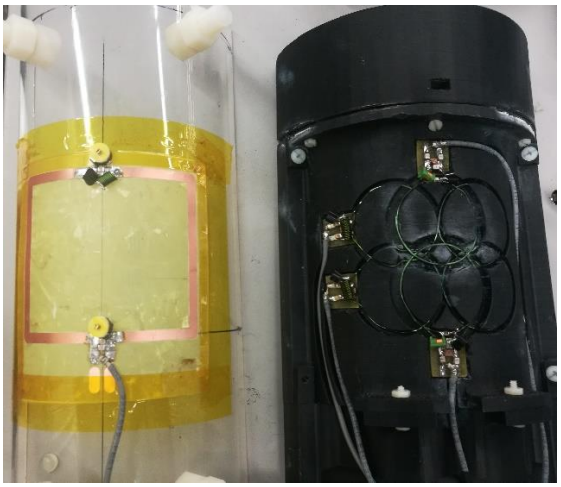

Fig. 21 The receiver four-element array, and a large 9cm×8cm loop coil that has the same overall size as the array as a comparison to the coil qualify factor and MRS SNR in the next chapter.

A comparison of a different number of turns loop coils shows that two turns coil gives better-loaded quality factor (Q_L) than one turn loop coil. The Q_L/ Q_{UL} ratio is close to 1 for one/two turn and figure 8, which means the noise source is mainly coil dominated for them, which is typical for the low field small loop coil.

As expected at low field, an increasing number of turns of the coil can increase the coil's sensitively by reducing the percentage of coil ohm's loss verse the phantom sample which is unavoidable. Also, the soldering joint and distributed capacitors' ohm loss also contribute a large portion of the coil's ohm loss. The ohm loss caused by the coil's wire and lamp elements are the dominated noise source for the low field coil, which is very different from the high field, where sample noise is easily dominated and only $\frac{B_1}{\sqrt{SAR}}$ need to be considered.

9cm × 8cm large loop coil has the lowest Q_L/ Q_{UL}. This is because a larger coil tends to have

sample dominated noise source. Two turns wire with a distributed capacitor is chosen to make the loop coil because of the measurement and fabrication convenience.

The author also finds that using AWG (America wire gauge) 21 copper wire to make two turns loop gives better quality factor than using the 1oz copper clad board (35.56 μm) with 2.35mm coil trace width. This is because, at 17.24 MHz, the skin deep is $\delta = \sqrt{\frac{2\rho}{\omega\mu}} = 15.7$ μm. At least 6 × the skin depth is needed to reduce the ohm loss $R_s = \frac{\rho L}{W\delta}$ of the strip line, ρ is resistivity, L is the wire length, W is the strip trace width and δ is the skin depth.The comparison between different wire gauge shows that AWG 17 two turns loop coil has slightly higher Q_{UL} but not improvement of Q_L is found.

The above experiments and measurements lead us to the conclusion that using wire that has diameters much larger than skin depth is better than the thin copper clad board. And multiply turns is necessary for low field receiver coil. The final design is a two-turn loop coil, and a one-turn figure 8 coil considering both SNR and fabrication convenience.

It is also found that smaller size coil has a larger Q_L/ Q_{UL} ratio compared with the larger coil. This indicates the coil source of a smaller coil will easily be coil dominated. This is expected [10], since smaller coil will have smaller sensitive region. It raises a question whether using an array of a smaller coil can achieve better SNR or not compared with a single larger coil. And this was later verified by the phantom experiment in the next chapter. It turns out that the linewidth of MRS also needs to be considered for SNR in the case of an inhomogeneous magnet.

References

[1] Barberi, E. A., Gati, J. S., Rutt, B. K., & Menon, R. S. (2000). A transmit-only/receive-only (TORO) RF system for high-field MRI/MRS applications. Magnetic Resonance in Medicine: An Official Journal of the International Society for Magnetic Resonance in Medicine, 43(2), 284-289.

[2] Vaughan, J. T., & Griffiths, J. R. (Eds.). (2012). RF coils for MRI. John Wiley & Sons.

[3] Carlson, J. W. (1989). Power deposition and noise correlation in NMR samples. Magnetic resonance in medicine, 10(3), 399-403.

[4] Hyde, J. S., Jesmanowicz, A., Froncisz, W., Bruce Kneeland, J., Grist, T. M., & Campagna, N. F. (1986). Parallel image acquisition from noninteracting local coils. Journal of magnetic resonance, 70, 512-517.

[5] Roemer, P. B., Edelstein, W. A., Hayes, C. E., Souza, S. P., & Mueller, O. M. (1990). The NMR phased array. Magnetic resonance in medicine, 16(2), 192-225.

[6] Carlson, J. W. (1989). Power deposition and noise correlation in NMR samples. Magnetic resonance in medicine, 10(3), 399-403.

[7] Hardy, C. J., Bottomley, P. A., Rohling, K. W., & Roemer, P. B. (1992). An NMR phased array for human cardiac 31P spectroscopy. Magnetic resonance in medicine, 28(1), 54-64.

[8] Wright, S. M., & Wald, L. L. (1997). Theory and application of array coils in MR spectroscopy. NMR in Biomedicine: An International Journal Devoted to the Development and Application of Magnetic Resonance In Vivo, 10(8), 394-410.

[9] Von Morze, C., Tropp, J., Banerjee, S., Xu, D., Karpodinis, K., Carvajal, L., ... & Vigneron, D. B. (2007). An eight-channel, nonoverlapping phased array coil with capacitive decoupling for parallel MRI at 3 T. Concepts in Magnetic Resonance Part B: Magnetic Resonance Engineering: An Educational Journal, 31(1), 37-43.

[10] Kumar, A., Edelstein, W. A., & Bottomley, P. A. (2009). Noise figure limits for circular loop MR coils. Magnetic Resonance in Medicine: An Official Journal

[11] Minyu Gu, Travis Carrell, John Bosshard, Clayton L. Cruthirds, Nicolaas EP Deutz, Marielle PKJ Engelen, Mary P. McDougall, Steven M. Wright, Dynamic 31P MRS of Skeletal Muscle with a 1 Tesla Extremity Scanner Dynamic 31P MRS of Skeletal Muscle with a 1 Tesla Extremity Scanner, 2019 ISMRM

CHAPTER IV

EXPERIMENTS OF PHOSPHOROUS MRS

In this chapter, we focus on the experiments of conducting in vivo skeletal muscle ^{31}P Magnetic Resonance Spectroscopy (MRS) with the ONI extremity 1 Tesla scanner. We use the designed transmit-only birdcage, four-element receive coil array described in the last two chapters, and a custom RF transceiver to obtain dynamic ^{31}P MRS. A custom plantar flexion-extension exercise device was also developed to enable the patient's local exercise. We study the improvement of SNR and linewidth using the four-element array compared with a conventional single element loop coil. We also show that the static magnetic field shimming cost is significantly saved by replacing single channel large receive coil with smaller size multi-channel receive coil array. These improvements make the ATP and Pi chemical shift to be distinguishable and easily quantified. The phantom and in vivo result shows only four to sixteen averages are required to obtain one ^{31}P MRS, which is comparable to other much more expensive higher-field whole body magnet. The preliminary in vivo result of human skeletal muscle ^{31}P MRS is obtained to monitor the metabolism change of the volunteer's skeletal muscle during an 18-minute local exercise protocol.[11]

4.1 1T ONI Magnet and B0 Field Homogeneity

A 21 cm inner diameter x 50 cm long extremity 1 T magnet (ONI Medical Systems, Inc) is installed in Texas A&M University Magnetic Resonance System Lab with an in-house built non-magnetic foot-flexion exercise apparatus. It is designed to provide detailed images of the foot, ankle, knee, etc. It has passive shimming and three-channel gradient coils. This system does not have any spectroscopy function. The primary goal of this project is to establish the spectroscopy

function, primarily focusing on dynamic ^{31}P in vivo MRS to monitor skeleton muscle metabolism.

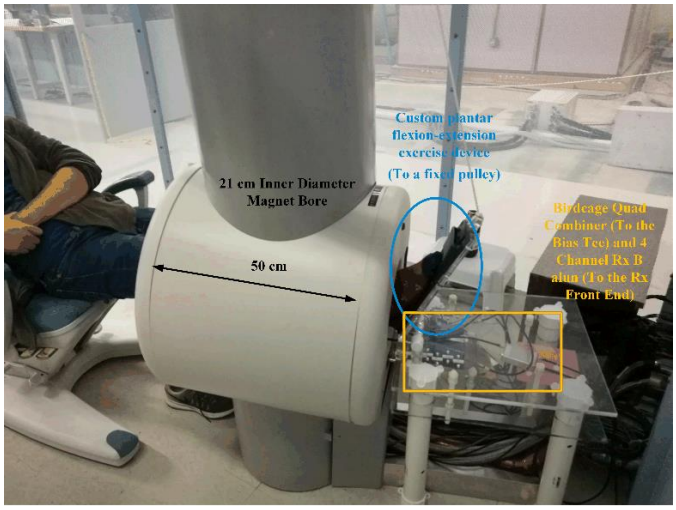

Fig. 22 ONI 1T extremity magnet and the custom plantar flexion-extension exercise device that can be used by subjects while inside the scanner in order to sufficiently stimulate the muscles of the lower leg (gastrocnemius, soleus, tibialis anterior). This device allows a custom weight to be used on a per-subject basis.

Besides the SNR issue, another factor obstructs ^{31}P MRS is the inhomogeneity of the static magnetic field. MRS usually requires a well-shimmed magnet. But this magnet is initially designed for imaging purpose, so it doesn't fully meet the spectroscopy's requirement of B_0 homogeneity. Fortunately, There is a relatively homogeneous region inside the magnet that can be used to conduct MRS.

To illustrate this, the ΔB_0 field map using a 90mm-diameter, the 17cm-length phantom is shown in the Fig. 23. Two groups of axial multiple slices gradient echo proton images using a 90mm diameter phantom with 10/30 ms echo time and 2100 ms repetition time are acquired. Each group of images contains 60 slices with 2mm slice thickness and no gap between them. FOV=160mm× 160mm and 128×128 resolution. The sequence is provided by ONI Orth-one. And the ΔB_0 field maps are calculated by

$$\Delta B_0 \text{ (ppm)} = \frac{\Delta\varphi}{\gamma B_0 \Delta TE} 10^6 \quad (4.1)$$

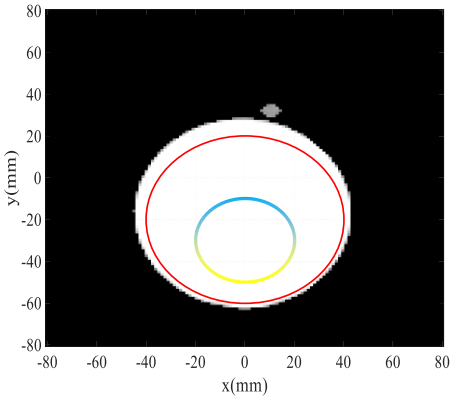

(a)

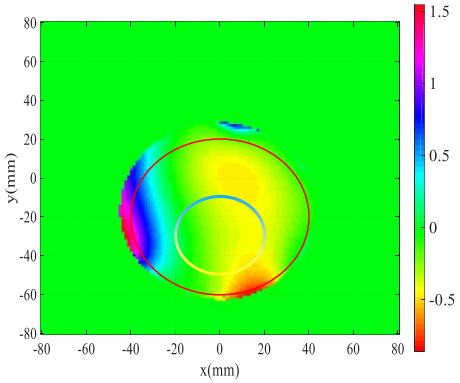

(b)

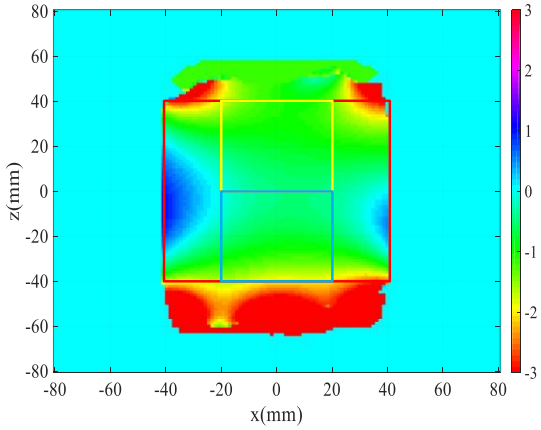

(c)

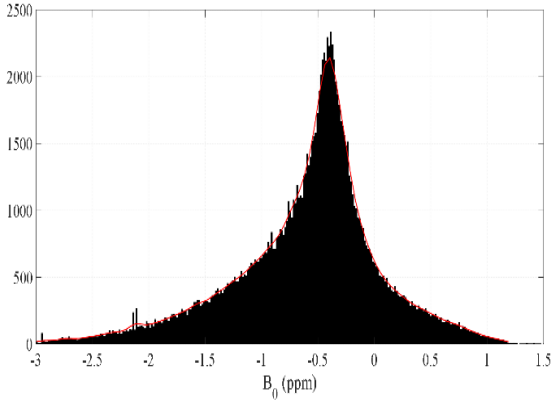

(d)

Fig. 23 (a) The axial gradient echo image of the central slice. The red circle stands for a 40mm radius, 80mm long cylinder region to cover the dimension of skeletal muscle. Yellow circle and the blue one shows the two separate relative homogeneous regions (b) The central axial slice ΔB0 map (c) The coronal central slice ΔB0 map (d) The histogram of ΔB0 (ppm) counted in the red cylinder region.

The phase along the different axial slices are found to be noncontinuous, so additional ΔB_0 map of coronal images are acquired to link the axial images' phase together. Before the multi-slice images are taken, Three-channel gradient shims are used to minimize the image volume's ΔB_0.

A ΔB_0 standard deviation of 0.671ppm is measured from a 40mm radius, 80mm long cylinder region (shown in red). The shape and dimension of this region are chosen to cover the whole human skeletal muscle's dimension. So if a volume coil or an over-size loop coil as RX mode are used, they lead to very bad linewidth.

To further minimize the linewidth received, we use an array of two pairs of loop and figure 8 coils to effectively breaks the relative homogeneous region of the B_0 field into two 20mm radius and 40mm length separate regions, shown in yellow and blue in Fig. 23. Each of which has a lower linewidth than would be seen by a large coil.

The yellow sub-regionΔB_0 stand deviation is measured to be 0.377ppm,and the blue one 0.472ppm. The local B_0homogeneity of each pair of figure 8 & loop will be better than the whole region so that linewidth for each channel is minimized. This two sub-region corresponds to each pair of the loop and figure 8 coil's sensitivity region. Thus, each channel of the array's received linewidth is better than a single coil of the same overall area which corresponds to the red region in the ΔB_0 map.

4.2 Spectrometer and Pulse Sequence Parameters

The OrthOne scanner does not support non-proton imaging or spectroscopy, nor the use of

array coils. Therefore, a prototype spectrometer built previously by others in the lab was used for this project. [1]

Non-localized spectroscopy pulse is used here to acquire ^{31}P MRS because the intrinsic signal and noise ratio (SNR) is the relatively low and high temporal resolution is desired for many in vivo metabolism researches. A broadband NMR spectrometer used for transmitting and receiving. For the spectroscopy experiments, hard pulse excitation was accomplished using an Analog Devices 9959 DDS, a four-channel 500 MSPS DDS with 10-bit amplitude and phase resolution. LabVIEW is used to program the pulse sequence design environment. The RF pulses are fed to a conventional 500w broadband amplifier. A 5v forwards/-15v reverse bias high-speed pin diode switch controlled by the console is used to tune/detune the transmit coil during transmit and receive window. A bias tee is used to combine the RF and DC first then fed to the coil. Receive coils are first connected to an Rx front-end which has first stage low noise amplifier (MITEQ AU-1583) and then to the second stage amplifier (Mini-Circuits GALI74). Then signals were filtered and directly digitized using an UltraView 16 bits 4 channels high-speed digitizer card. All signal Postprocessing was performed in MATLAB.

A 300us hard pulse is sent to the transmit coil. After 500 usec, 0.512s 4 channels' data are acquired with 50MSPS/ch sampling rate. Repetition time is 4s. 90-degree tip angle is calibrated with a phosphoric acid phantom and was found to be approximately 300 usec. The data was directly sampled at 50 MS/S and stored for digital demodulation into spectra following the study.

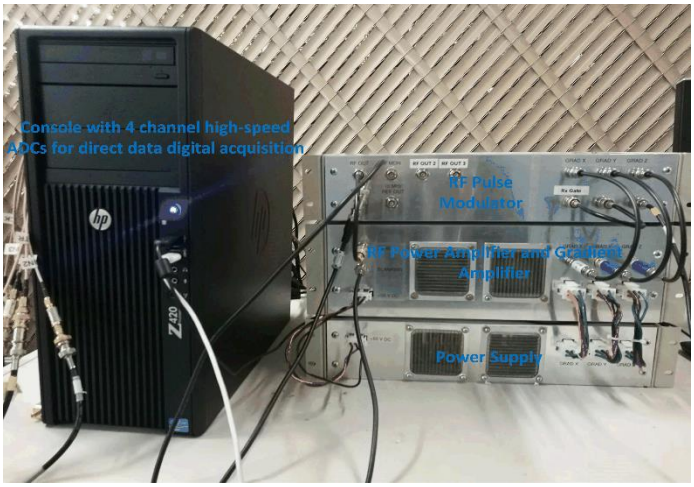

Fig. 24 The one-channel transmitting and four-channel receiving broadband NMR spectrometer.

4.3 Array Signal Processing

Averages are done simultaneously on each channel first. Then each channel is 0-order phase corrected to the PCr peak. Later the whole spectral is shifted to make the PCr peak at 0 ppm, which will align all channels' spectral peaks together. This step is necessary because the static magnetic field inhomogeneity may create central peak frequency shift for different channels, as shown in Fig. 25. Without shifting the peaks, the linewidth is a little worse, and some of the split peaks are not distinguishable. All channels' data are combined based on SNR weight,

$$w_i = \frac{SNR_i}{\sum SNRp_i} \quad i=1,2,3,4. \quad (4.2)$$

$$S_{acq}(f) = \sum_{i=1}^{4} w_i S_i(f) \quad (4.3)$$

The spectral domain SNR in NMR is commonly defined as

$$\text{SNR}=\frac{Peakareaintegral}{Noisedensity \times Peakbandwidth} \quad (4.4)$$

If the peaks are assumed to have Lorentzian line shape

$$\frac{a}{1+(\frac{f}{w/2})^2}, (4.5)$$

a is the peak height and w is the full width at half maximum. SNR is simplified to $\text{SNR} =$

$$\frac{\frac{aw\pi}{2}}{std(noise)*4w} (4.6)$$

peak bandwidth =2w and finally defined as

$$\text{SNR}=\frac{\max(MRS)}{std(noise)} (4.7)$$

The first order correction and baseline correction are applied afterwards if necessary. 3Hz line broadening is applied on the in vivo and ^{31}P physiological concentration phantom bottle but not on the phosphoric acid bottle.

When using weighted SNR measured in spectral domain to combined the array signal, linewidth issue is incorperated in the formular 4.7 descibed above. This is because a broad linewidth peak will results in lower peak height, presumely the signal amplitude in the time domain is the same.

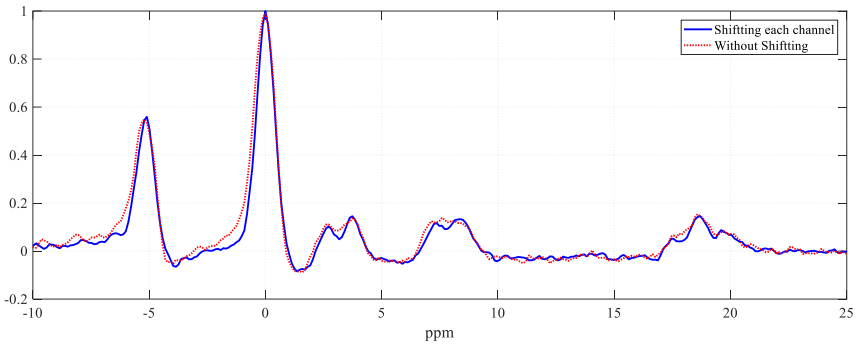

Fig. 25 The MRS of a ^{31}P physiological concentration phantom. Blue one shifts each channels' spectral so that their peaks are aligned together. The split peaks of ATP are distinguishable using this method. The read one shows the MRS which each channels' spectral is directly added together. In this case the peak linewidth is broader and the split peaks of ATP are not distinguishable anymore. This indicates by shifting each channels' spectral, a better linewidth of smaller loop coil is mantained.

4.4 85% Phosphoric Acid Phantom ^{31}P MRS

An 85% phosphoric acid bottle which has 12cm length and 7cm diameter is used as a phantom for 90-degree power calibration and shimming adjustment because it provides very high concentration ^{31}P nuclear so that the calibration can be stable. Phantom phosphorus scans were acquired at 17.24 MHz (repetition time = 4 s, sampling rate = 50 MSPS/channel for 4 channels, acquisition time = 0.512 s, number of points=5120).

Three channel gradient shims are adjusted to minimize the linewidth of Loop I&II. Due to the figure-8 sensitivity region overlapping the loop coil, the shims were adjusted to minimize the line width difference on both Loops I & II in order to obtain a similar signal and noise level for each channel which result in an optimal combined result of the array. Shim settings obtained from this step were used for the remaining phantom test and *in vivo* study. The shim was readjusted when using the single element large coil as the receiver.

The conductivity of phosphoric acid is much higher than the human body. So, it loads the coil differently compared with a real human subject. There will be more noise from the sample. Nerveless, it still can be used to estimate the linewidth of ROI.

From table 4, channel 1 and 2 have better linewidth and SNR than channel 3 and 4. This is because the static magnetic field is more homogeneous at the spot where channel 1 and 2 are located at. This means the position of the coil may affect the SNR performance. The array combined SNR is 1.72 × better than the four channels' average SNR. The combined linewidth is kept as a minimum level too.

The large loop coil is tested to compare with the coil array. It has the same overall size (9cm×8cm) as the coil array. The array's 4-channels combined result improves the linewidth from 0.71ppm to 0.38ppm. This is because each smaller coil detects a smaller area of the sample and the linewidth of array combined result after aligning the peaks and correct the phase is much better than the large loop coil's. A larger coil will have worse linewidth and eventually fails to make the spectral peak distinguishable, while the array can recover linewidth and solve this issue. The disadvantage of the smaller coil is its overall signal detected is much less than a larger coil's, so multiple array elements are used here to resolve this problem.

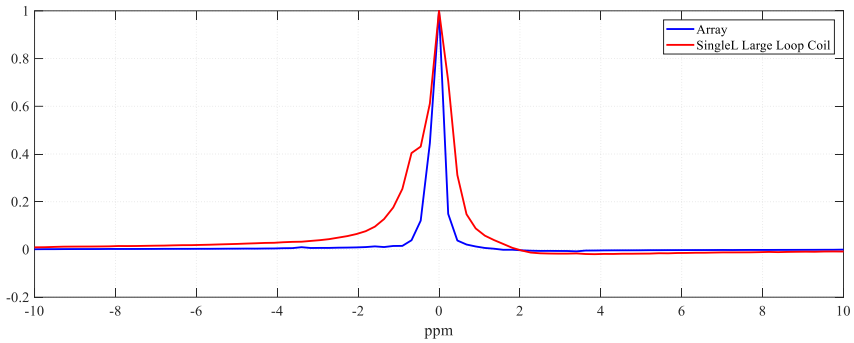

Fig. 26 The normalized MRS of a phosphoric acid phantom. One average is acquired. Blue one is the result of combing 4-channels signal, linewidth =0.33ppm is found. The red one is the result of the single large loop, and linewidth=0.71ppm.

Table 4 Coil Performance of Phosphoric Acid Phantom

	SNR	**Linewidth(ppm)**
Channel 1: Loop	6413	0.29
Channel 2: Figure 8	6415	0.29
Channel 3: loop	4267	0.45
Channel 4: figure 8	4750	0.38
Array combined	9392	0.33
The single large Loop coil	4967	0.71

4.5 Physiological Concentration ^{31}P Phantom MRS

A physiological concentration ^{31}P phantom is made with 34mmol/L phosphocreatine, 8.1mmol/L ATP, 4.6mmol/L Pi and 0.5mg sodium azide to provide PCr, Pi, and three ATP peaks which simulates in vivo human skeletal muscle condition. Conductivity is found to be 0.95s/m which is close to in vivo 0.7 s/m. 4 averages with 4s TR are acquired to validate the system's feasibility, other scan parameters are the same as the phosphoric acid scan.

From fig. 27 (b) The MRS obtained with 4 averages using the array is clear, and all the split peaks of ATP are distinguishable. Table 4 shows the detailed PCr SNR and linewidth of 4 channels' MRS. All the measurements in the table 4 and in vivo MRS in the next section are taken without the line broadening. All four channels receive similar SNR and linewidth. Array combined SNR is 2.1 × better than the four-channel average SNR. The noise correlation between channels is less than 6%, which is because the noise source is coil dominated.

By comparison to the 9cm×7.875cm single large coil, PCr's SNR using the array is 1.8× better than single large loop coil's, and the linewidth measured from PCr peak is 0.72 ppm, which is 1.7× the array's. ATP peaks are not clearly distinguishable due to the poor linewidth. The physiological phantom result shows the promising feasibility of this system for conducting dynamic ^{31}P in vivo MRS with a reasonable time resolution and shows its advantage over conventional single coil design.

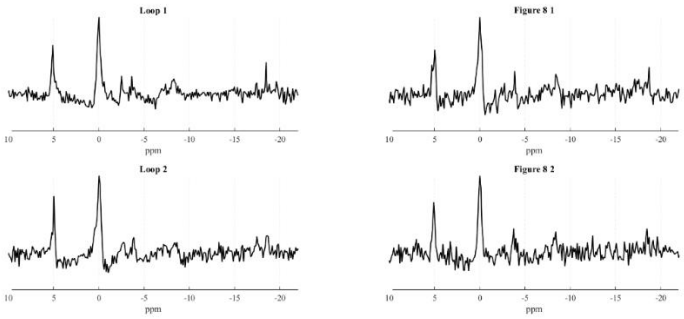

(a)

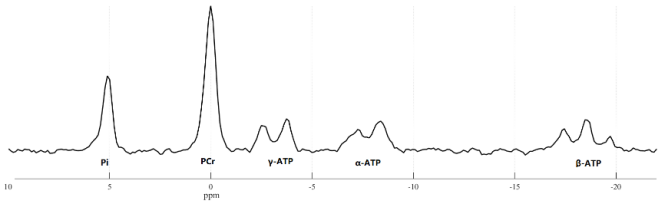

(b)

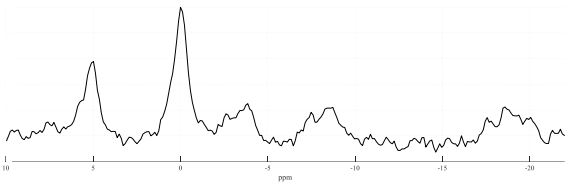

(c)

Fig. 27 The MRS of a physiological concentration 31P phantom result. 4 averages are acquired. (a) is the spectrum of each channel, (b) is the combined 4 channels MRS with 3Hz line broadening (c) is the MRS of single large Loop coil with a 3Hz line broadening as a comparison. The use of the array provided a significant linewidth improvement from 0.72 ppm to 0.45 ppm. The linewidth improvements stem from each channel detecting a smaller area of the sample, and the factor that B0 field is more homogeneous in a smaller region.

Table 5 Coil Performance of Physiological Concentration ^{31}P Phantom

	PCr SNR	PCr Linewidth (ppm)
Channel 1: Loop I	18.0	0.44
Channel 2: Figure 8 I	15.4	0.45
Channel 3: Loop II	17.6	0.45
Channel 4: Figure 8 II	12.7	0.42
Array Combined	33.6	0.45
Single Large Loop Coil	18.6	0.72

These improvements stem from each channel detecting a smaller area of the, as well as the array combination. The array's function for recovering linewidth and improving SNR has been demonstrated. The multi-element system was able to recover the linewidth and resolve this issue without the need for low-impedance decoupling preamplifiers. This is an essential aspect for an inexpensive, widely deployable system where patient-specific shimming is likely to be very limited.

4.6 In Vivo ^{31}P MRS

A healthy female volunteer underwent a 6-minute static foot local exercise protocol for monitoring the metabolism within the skeletal muscle. The patient was directed to apply and maintain plantar flexion against a custom foot flexion device weighted with 15lb. 90 acquisitions were obtained before, during, and after the exercise protocol. TR=4S, acquisition time=0.512s,

number of points=5120. Tip angle is reduced to 60 degree to obtain a stronger PCr signal due to partial T1 relaxation. And 3 dummy scans were taken before recording the data.

In the baseline data, the first eight average SNR of PCr was 42.14 and Pi was 6.59. The combined linewidth was measured as 0.41 ppm (measured before line broadening). If the number of average is increased to sixteen, the SNR of PCr was increased to 59.1and Pi's was 8.87 as expected. An eight-average sliding averaging of the whole 18-minute protocol is shown in Fig.28 a. The split peaks of ATPs are visible, but the γ-ATP peak partially overlaps with PCr peak. This creates difficulty of accurate quantification using PCr peak's area integration. Sixteen averages were utilized for obtaining a reliable SNR for quantifying and monitoring the PCr, Pi. The characteristic decrease in PCr and increase in Pi at the beginning stage of the local exercise was observed for the *in vivo* spectra shown in Fig. 28. In the recovery stage, the exercise was stopped, and Pi/PCr ratio gradually decrease.

Next, we investigate utilizing the spectral peak integration to quantify the metabolism. The peaks area of the metabolism is chosen based on 90% of the peak height(within a fixed range of the peak chosen based on the baseline averaged result). For PCr peak integration, the part that overlaps with the γ-ATP peak is not included. The result of PCr, Pi peak integration ratio are shown in Fig. 28 c. It is found that the integration result mostly overlaps with the peak height's result, but the PCr peak integration's value changes less than with peak height, which is due to the linewidth change of PCr during the exercise.

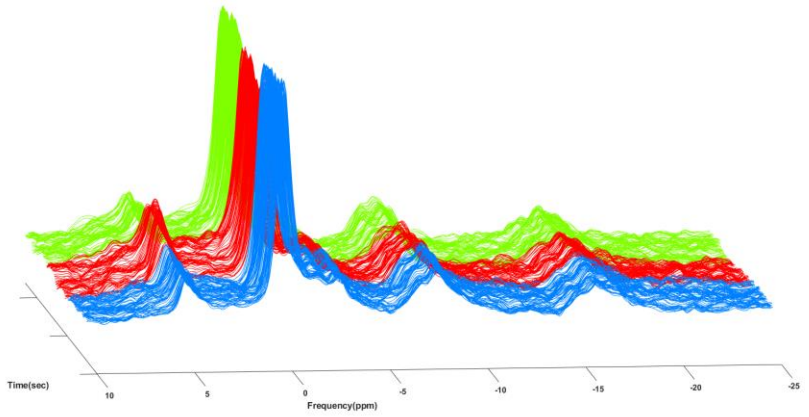

(a)

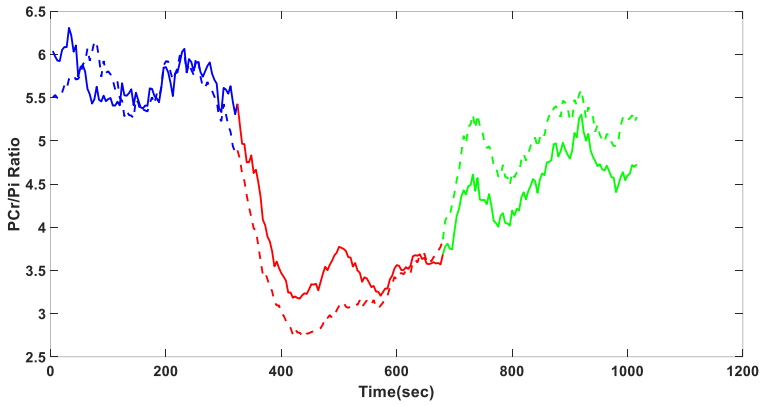

(b)

Fig. 28 (a) The in vivo ^{31}P skeletal muscle ^{31}P MRS of a volunteer during eighteen minutes' protocol, sliding average with 8-average window and 8Hz line broadening are used here. (b) The peak height (dash line) and The peak integration (solid line) of PCr and Pi throughout the baseline (blue), exercise (red), and recovery (green). A 16-average sliding window average and 8 Hz line broadening were used for each spectrum.

For the baseline result of the first 12 averages, the pH level of 7.02 was within literature reported ranges. Although the T1 partial saturation corrected PCr/Pi ratio of 6.62 (T_1 partial saturation factor 1.0349) was also within values reported with the literature [8]. We find from the in vivo result that accurate quantification of Pi peak is challenging due to the low SNR peak of Pi during the baseline and exercise phase. But due to the low SNR of ATP peaks. and split peaks are not well separated after linebroading. The ATP peak integration gives an unreliable result, thus not utilized here. Further improvement of linewidth and SNR are needed to enable a more robust ATP peaks' quantification.

4.7 The Benefit of Increasing Array Elements

The array's function of recovering linewidth and improving SNR has been shown here. For the initial investigation of feasibility reported here, we implement a four-element array to cover the most homogeneous region of the magnet. To further explore the necessity of increasing array elements, A possible modeling method taking the static magnetic field, load sample shape, and coils into consideration is discussed here.

To predict the linewidth of each channel's received MRS, one can numerically simulate MRS based on the ΔB0 map and the coil B_1 profile. To do so, the time domain signal is first calculated by

$$\text{Signal} = \iiint_{\Omega} \omega\overrightarrow{B_1} \cdot \overrightarrow{M_{xy}}\, e^{j\gamma\Delta B_0 t} e^{\frac{-t}{t_2}} d\Omega \quad (4.8)$$

γ is the Larmor frequency, t2 is chosen as 354ms which approximates the PCr's value [2], the constant transverse magnetization $\overrightarrow{M_{xy}} = M_0\vec{x}$is assumed here. Ω stands for the red cylinder region mentioned in fig 2. The numerical integral is done by discretizing this region into 1.25mm×1.25mm×2mm cells. The $B_1$is calculated from the numerical integral of Biot–Savart law assuming constant current density on the coil. The formula is simplified to

$$\text{MRS} = \text{FFT}(\sum_i \sum_j \sum_k \omega B_z(i,j,k) M_0 \, e^{j\gamma \Delta B_0(i,j,k)t} e^{\frac{-t}{t_2}}) \quad (4.9)$$

Then to compute the SNR, we use

$$\text{SNR} = \frac{\max(MRS)}{\sqrt{4KT(R_S+R_C)}} \quad (4.10)$$

the MRS is obtained by equation (4.9), R_s sample loss is retrieved from the RemCom XFDTD EM simulation. The real part of the coil simulated input impedance is used as the sample loss. Rc is calculated from $\frac{\rho}{\delta}(\frac{L}{\pi D})$, the ρ is the copper resistivity, δ is the skin depth, L is the wire length, and D is the wire diameters. The solder joint and capacitor loss are not considered here which might vary from different designs and fabrications.

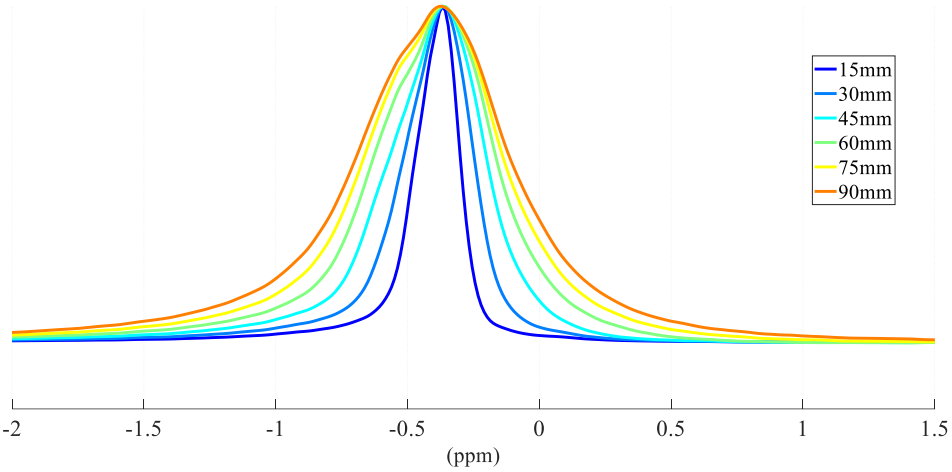

(a)

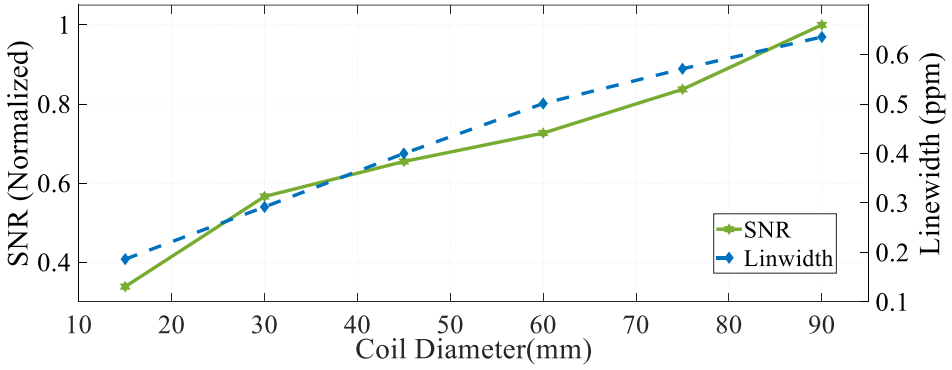

(b)

Fig.29 (a) Simulated MRS using different loop coil diameters (b) Blue line shows the normalized SNR evaluation of non-localized MRS verse the loop coil OD. The green line shows the linewidth result.

Fig. 29 gives result MRS swapping different coil diameters from 15mm to 90mm. The 90 mm one's sensitivity region covers the whole cylinder and should provide a better SNR regardless of the B0 inhomogeneity. It's found here that it leads to 0.64 ppm linewidth. The 45 mm OD one gives 0.4 ppm linewidth. Those results match the physiological concentration of phantom's experiment.

We can also predict that if we further increase the array elements to 16 and reduce the single element's diameter to 22.5mm. The 16-elements combined SNR will be 1.38 times better than the 4-element and linewidth will be reduced to 0.24ppm. Due to the fact that noise source is coil dominated, increasing array elements will be less beneficial to SNR but will significantly improve linewidth. This improvement of linewidth is significant for the robust quantification of the spectral peak, especially when the signal and noise ratio is low.

4.8 ^{31}P MRS Time Domain Quantification

The purpose of MRS quantification is to accurately find the T_1, T_2^*, resonance amplitude, chemical shift frequency from the FID/echo signal. In the ^{31}P MRS study, people mainly focus on finding the amplitude of Pi, PCr peak, and the chemical shift of these two peaks. The most straightforward method to quantify the peak is to find the spectral domain peak area integration and use this value as the amplitude of this resonance peak. This method has unsatisfying robustness when the SNR is low, and may not work when the spectrum has the baseline distortion or overlapping peaks caused by B_0 field inhomogeneity. Another issue is subjective of human interface and lack of consistency. Thus, many algorisms have been developed to conduct the automatic quantification of MRS[3][4]. Here we use the algorisms developed from linear predictive theory[5][6], which is a time domain least square approach for the parameter estimation of damped sinusoids.

The N-point Fid formed by K exponentially damped sinusoid signal of a sampling interval Δt can be expressed by

$$x_n = x(n\Delta t) = \sum_{k=1}^{K} c_k e^{-b_k n\Delta t} e^{-j(\omega_k n\Delta t+\varphi_k)} + w_n \quad (4.11)$$

The w_n represents white noise. By invoking the principle if linear prediction, one can fitting equation (4.11) to the real FID signal. We first assume that each data point can be expressed as a linear combination of the M previous ones, which is formulated by

$$x_n = a_1 x_{n-1} + a_2 x_{n-2} + \cdots + a_M x_{n-M} (4.12)$$

The n is taken from M to N-1. This is called backward linear prediction, which each point is determined by its previous M point of data. A (N-M) × M Hankel matrix can be used to represent this

$$H = \begin{pmatrix} x_1 & x_2 & \cdots & x_M \\ x_2 & x_3 & \cdots & x_{M+1} \\ \vdots & \vdots & \ddots & \vdots \\ x_{N-M} & x_{N-M+2} & \cdots & x_{N-1} \end{pmatrix}, (4.13)$$

$$A = \begin{pmatrix} a_1 \\ a_2 \\ \vdots \\ a_M \end{pmatrix}, (4.14)$$

$$X = \begin{pmatrix} x_{M+1} \\ x_{M+2} \\ \vdots \\ x_N \end{pmatrix}, (4.15)$$

$$X = HA. (4.16)$$

A can be found by inverting the matrix H, and the solution produces an estimation of X minimized the sum of square differences between original and estimation. Matrix SVD (Singular value decomposition) can be used to find its solution and filter out the noise in the original signal.

$$H_{N-M,M} = U_{N-M,N-M} S_{N-M,M} V_{M,M} (4.17)$$

The S is a diagonal matrix which contains harmonic components in FID signal in order from dominant to negligible. The noise which has negligible value in S compared to the harmonic components can be filtered by truncating the S to a square matrix of order F, and cut off columns of U,rows of V.

$$H_{N-M,M} = U_{N-M,F} S_{F,F} V_{F,M} \quad (4.18)$$

$$inv(H_{N-M,M}) = V_{M,F} S_{F,F} U_{F,N-M} \quad (4.19)$$

$$A_M = V_{M,F} S_{F,F} U_{F,N-M} X_{N-M} \quad (4.20)$$

After the A is computed, plug the linear prediction coefficients a_M back to equation (4.12) , this leads to

$$z^M - a_1 z^{M-1} \ldots - a_M z^0 = 0 \quad (4.21)$$

The kth root z of this equation (4.21) represents $e^{-b_k \Delta t} e^{-j\omega_k \Delta t}$, only those roots that are located inside the unit circle of complex plane stands for the damping harmonic components. The frequency and damping can be found by

$$\omega_k = \frac{-angle(z_k)}{\Delta t} \quad (4.22)$$

$$\alpha_k = \frac{1}{abs(z_k)\Delta t} \quad (4.23)$$

To retrieve the amplitude of the harmonic components, we construct a harmonic basis matrix

$$b_n = b(n\Delta t) = e^{-b_k n\Delta t} e^{-j(\omega_k n\Delta t + \varphi_k)} \quad (4.24)$$

$$B = \begin{pmatrix} b_1 \\ b_2 \\ \vdots \\ b_F \end{pmatrix} \quad (4.25)$$

$$\mathrm{Fid} = \mathrm{B} * \mathrm{Amp}(4.26)$$

And the amplitude vector can be found by inverting this matrix. This can be done by using the SVD again.

To test the function of LPSVD, we simulated three sine waves, with input parameters

Table 7 Input Simulated Sine Waves

Frequency (Hz)	Damping (Hz)	Complex Amplitude
-10	3.502	1
50	7.005	1
100	7.005	1

and white noise is added to make the SNR 9.5db. The result of LVSVD are

Table 8 LPSVD Result of Simulated Sine Waves

Frequency (Hz)	Damping (Hz)	Complex Amplitude
-9.961	3.679	0.900 + 0.00341i
49.926	11.623	1.296 + 0.108i
100.338	9.349	1.05 - 0.0409i

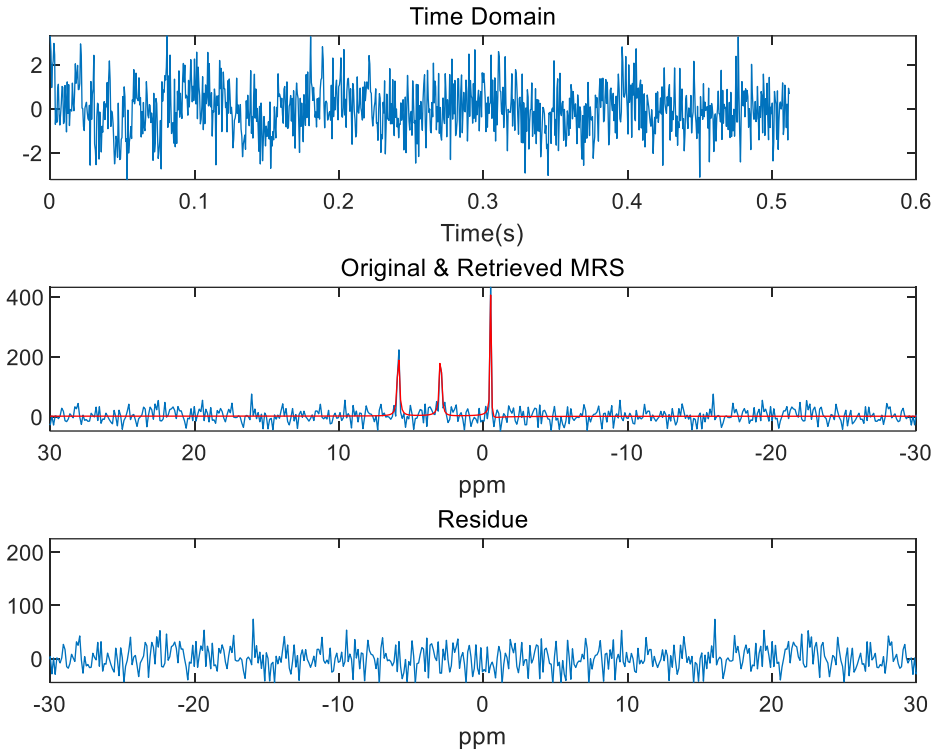

Fig. 30 The time/frequency domain of original simulated FID (blue) and the result retrieved by LPSVD (red).

In vivo ^{31}P MRS data taken from volunteer's skeletal muscle is also tried using LPSVD. 8 averages with 6 Hz line broadening and phase were applied as pre-processing. The code was asked to looking for 5 harmonic components.

Table 9 LPSVD Result of In Vivo Data

Frequency (Hz)	Damping (Hz)	Complex Amplitude
0.9675	62.779	11584 + 577i
-37.121	35.601	1425 - 349i
79.921	66.874	1966 + 1119i
-127.837	100.119	4510 - 1255i
-282.982	114.989	4278 - 173i

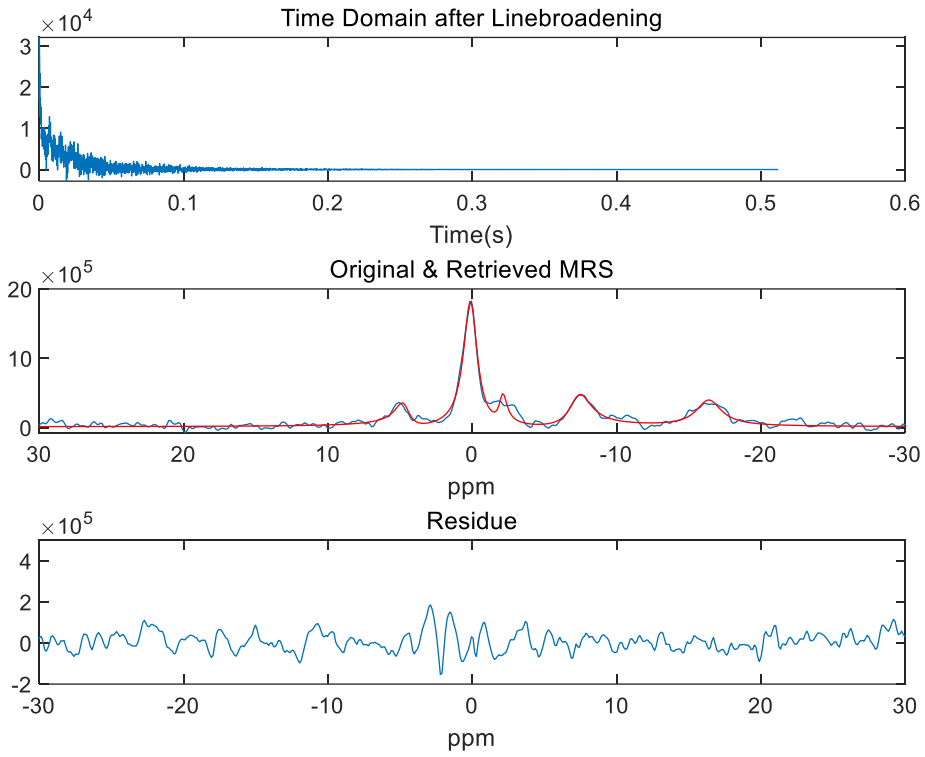

Fig.31 The time/frequency domain of original FID and the result retrieved by LPSVD.

In practice, when using the time domain quantification method like LPSVD, it fits well to the high SNR peaks like PCR. But for the low SNR peaks (SNR<10) like ATP and Pi, the fitting reveals the error. This is very obvious when the linewidth is broad, and the peak height is close

to the noise floor. The splitting peak of ATP peaks creates more difficulties for fitting it well. Thus, like expected, to obtain a reliable quantification of MRS, the original MRS SNR is the most critical factor to pursue even with the help of the fitting algorisms.

References

[1] Stephen Ogier , John C Bosshard , and Steven M Wright, A Broadband Spectrometer for Simultaneous Multinuclear Magnetic Resonance Imaging and Spectroscopy, 2016 ISMRM

[2] B. R. Newcomer and M. D. Boska, "T1 Measurements of 31 P Metabolites in Resting and Exercising Human Gastrocnemius/Soleus Muscle at 1.5 Tesla," Magnetic Resonance in Medicine, no. 41, pp. 486-494, 1999.

[3] Stefan, D. D. C. F., Di Cesare, F., Andrasescu, A., Popa, E., Lazariev, A., Vescovo, E., ... & Van Ormondt, D. (2009). Quantitation of magnetic resonance spectroscopy signals: the jMRUI software package. Measurement Science and Technology, 20(10), 104035.

[4] Vanhamme, L., Van Huffel, S., Van Hecke, P., & van Ormondt, D. (1999). Time-domain quantification of series of biomedical magnetic resonance spectroscopy signals. Journal of Magnetic Resonance, 140(1), 120-130.

[5] Tufts, D., &Kumaresan, R. (1982). Singular value decomposition and improved frequency estimation using linear prediction. IEEE Transactions on Acoustics, Speech, and Signal Processing, 30(4), 671-675.

[6] Barkhuijsen, H., De Beer, R., Bovee, W. M. M. J., Creyghton, J. H. N., & Van Ormondt, D. (1985). Application of linear prediction and singular value decomposition (LPSVD) to determine NMR frequencies and intensities from the FID. Magnetic resonance in medicine, 2(1), 86-89.

[7] Vanhamme, L., van den Boogaart, A., & Van Huffel, S. (1997). Improved method for accurate and efficient quantification of MRS data with use of prior knowledge. Journal of magnetic resonance, 129(1), 35-43.

[8] B. Chance, J. Im, S. Nioka, and M. Kushmerick, "Skeletal muscle energetics with PNMR:

Personal views and historic perspectives," NMR in Biomedicine, vol. 19, no. 7, pp. 904-926, Nov 2006.

[9] A. I. Schmid et al., "Exercising calf muscle T2*changes correlate with pH, PCr recovery and maximum oxidative phosphorylation," NMR in Biomedicine, vol. 27, no. 5, pp. 553-560, 2014.

[10] Minyu Gu, Travis Carrell, John Bosshard, Clayton L. Cruthirds, Nicolaas EP Deutz, Marielle PKJ Engelen, Mary P. McDougall, Steven M. Wright, Dynamic 31P MRS of Skeletal Muscle with a 1 Tesla Extremity Scanner Dynamic 31P MRS of Skeletal Muscle with a 1 Tesla Extremity Scanner, 2019 ISMRM

CHAPTER V

CONCLUSION AND FUTURE WORK

The feasibility of conducting dynamic in vivo ^{31}P MRS in a low-cost extremity 1T scanner is validated. We design and build a transmit-only birdcage, four-element receive coil array and RF transceiver to improve the SNR and recover the linewidth. The studies of the transmitter volume coil show that birdcage coil has much higher efficiency than saddle coil and is preferred as a transmitter coil for the low field NMR when the power budget has constraints. A new configuration of four-element receiver coil array is proposed here, which is optimized for high SNR at low field, and compact overall size due to magnetic inhomogeneity. The array is found to obtain 2.1 × better SNR than a single channel. The function of the array to recover the linewidth is discussed here, and the linewidth is improved from 0.72 ppm to 0.45 ppm compared with a large loop coil with the same overall size. The static magnetic field shimming procedure is significantly simplified by replacing single channel large receive coil with smaller size multi-channel receive coil array. These improvements make the ATP and Pi chemical shift to be distinguishable and easily quantified. The phantom and in vivo result shows only four to sixteen averages are required to obtain one ^{31}P MRS, which is comparable to other much more expensive higher-field whole body magnet. The initial in vivo result of human skeletal muscle ^{31}P MRS successfully monitors the metabolism change of the volunteer's skeletal muscle during an 18-minute local exercise protocol.

The initial experiments done here shows a promising future to use 1T low-field extremity scanner as a low-cost platform for various in vivo ^{31}P spectroscopy studies. The work I did during the master were mostly focusing on the hardware's perspective. Many other improvements can be made to make ^{31}P MRS even faster / more reliable at 1T, besides increasing the array's elements described in chapter 4. Here only 90-degree hard pulse is used as a pulse sequence. A more

profound choice of tip angle, repetition time, pulse sequence and post-processing using prior knowledge of in vivo ^{31}P MRS can furthermore enhance the time resolution. The linewidth and SNR performance of the array is simulated and tested by a liquid phantom. In the real human subject, the inhomogeneous susceptibility and fat layer vary from different persons. Those factors will affect the linewidth and SNR which should be included in the future work. The noise is found to be coil dominated for the array element, which indicates an improvement of sensitivity can still be achieved by, for example, increasing coil turns. But this will create practical array fabrication difficulty. Using superconducting coil, or reducing coil temperature could also significantly reduce the coil loss. The challenge of implementing these technologies, especially in a limited space of magnet bore, is patient safety. The research of the magnetic guide could be an approach to this problem [1]. We are also building a dual-tune ^{31}P/^{1}H coil to enable nuclear overhauser[2]. All in all, 1T extremity scanner shows its infinite potentials for conducting various MRS research with a low-cost solution.

References

[1] Wiltshire, M. C. K., Pendry, J. B., Young, I. R., Larkman, D. J., Gilderdale, D. J., &Hajnal, J. V. (2001). Microstructured magnetic materials for RF flux guides in magnetic resonance imaging. Science, 291(5505), 849-851.

[2] Neuhaus, D. (2007). Nuclear overhauser effect. eMagRes.

APPENDIX A

MATLAB CODE FOR ARRAY SIGNAL PROCESSING

```
% This code demodulates 4-channel data from Ultra-View Acquisition Card and
combine different channels' signal by SNR weight. It saves all the FID
to .mat file. It also supports basic MRS pre-processing routines like 0/1
order phasing, line broadening, baseline correction(additional function
needed), SNR calculation.

% Output format Num of scan * Num of point mat file or txt file read by
JMRUI.


%% process raw data
file='...';
num_ch=4;
CD=fs*at*num_ch;
noise_region=1/10;
%set the base band bandwidth at 17.24mhz
fs=50e6;
Nacq=12;
f0=17.2398e6;
at=0.512;
np=round(fs*at);
df=1/at;
bw=10*10^3;
var_pts=round(bw/df);

%Read in Ultraview binary data

% find fiducial spacing
FID=fopen([file '.dat'],'r','l');

% find first fiducial location
A=fread(FID,100000,'uint16');


% the fiducial is a data pattern formed by 4 number
fidupat=[0 1 65535 65534];
loc=strfind(A',fidupat);

% find other fiducial locations (look around -2000 points where they should
be based on CD)
% Note fseek moves in 1-byte steps, while fread moves in 2-byte steps
% because it is uint16

if Nacq==1
    loc(2)=CD+1;
else
    for acq=2:Nacq
         %because CD may not be the acutal data length of one acq,first we
        %use CD to find out length
```

```
        if acq==2
            startpoint=CD;
            fseek(FID,(startpoint-2000)*2,-1);
            %then we used the found length loc(2)-loc(1) as start point of
            %one acq
        elseif acq>2
            startpoint=(loc(2)-loc(1))*(acq-1);
            fseek(FID,(startpoint-2000)*2,-1);
        end
        A=fread(FID,10000,'uint16');
        place=strfind(A',fidupat);
        loc(acq)=place+startpoint-2000;
    end
end
acqsizes=diff(loc)-4;   %subtract 4 for fiducial length;
len=min(acqsizes)/num_ch;

tavg=zeros(4,len);

for acq=1:Nacq

    fseek(FID,(loc(acq)-1)*2,-1);
    fidu=fread(FID,4,'uint16');
    if fidu==[0;1;65535;65534];
        disp(['Acquisition Number ' num2str(acq)]);
    else
        disp(['Acquisition Number ' num2str(acq) 'Error in Parsing']);
    end

    %
    A=fread(FID,len*num_ch,'uint16')-32768;

    % reshape a multi channel acq
    A=reshape(A,[num_ch,len]);

   tavg(1,:)=tavg(1,:)+A(1,1:(len));
   tavg(2,:)=tavg(2,:)+A(2,1:(len));
   tavg(3,:)=tavg(3,:)+A(3,1:(len));
   tavg(4,:)=tavg(4,:)+A(4,1:(len));

end


%% truncate or zero filling
ppm_left=-10;
ppm_right=25;

disp('input 0 if you want to truncate half of the signal to 0, input 1 if you
want to zero filling')
indicator=input('indicator:');


if indicator==0
    % set the half data to 0;
```

```
tavg(:,round(length(tavg(1,:))/2):end)=zeros(4,round(length(tavg(1,:))/2));
elseif indicator==1
    % double the tacq to make the fft resolution better
    tavg_zf=zeros(num_ch,length(tavg(1,:))*2);
    for i=1:num_ch
        tavg_zf(i,:)=[tavg(i,:) linspace(0,0,length(tavg(i,:)))];
    end
    % zero filling
    at=at*2;
    np=round(fs*at);
    % recalculate the base band bandwidth at 17.23mhz
    df=1/at;
    bw=10*10^3;
    var_pts=round(bw/df);
    len=len*2;
    tavg=tavg_zf;
end

faxis=linspace(-df*(var_pts/2-1),df*(var_pts/2),var_pts)/f0*10^6;
spectrumadd=zeros(1,var_pts);
noise_array=zeros(4,var_pts*noise_region);

disp('input 1 to find the peak based on the defaut MRS center frequency')
cf=input('cf:');

%% baseband
for i=1:num_ch
spectavg=fftshift(fft(tavg(i,:)));
% plot baseband in ppm, get peak
spectrum=spectavg(round(len/2+round(f0/df)-(var_pts/2-
1)):round((len/2+round(f0/df)+(var_pts/2))));
if cf==1
    maxnum=2546;
    [maxvalue,maxnum]=max(abs(spectrum(maxnum-200:maxnum+200)));
    maxnum=2546-200+maxnum-1;
else
    [maxvalue,maxnum]=max(abs(spectrum));
end

% SNR and noise
noise=std(real(spectrum(1:var_pts*noise_region)));
noise_array(i,:)=real(spectrum(1:(var_pts*noise_region)));
SNR=maxvalue/noise*0.655;
disp(strcat('c',num2str(i),' signal:',num2str(maxvalue),'
noise:',num2str(noise),' snr:',num2str(SNR)));
disp(strcat('maxnum: ',num2str(maxnum)));

% 0 order phase, normalized to the main peak
spectrum=spectrum.*conj(spectrum(maxnum))/maxvalue^2;

% put the main peak at center of the spectra
spectrum=circshift(spectrum',round(var_pts/2-maxnum+1));
spectrum=fliplr(spectrum');
```

```
% plot the normalized MRS
figure;
plot(faxis,real(spectrum));
xlabel('ppm');
title(strcat(file,'_c',num2str(i)),'Interpreter', 'none');
xlim([ppm_left ppm_right]);

% add the different channels MRS based on weighted SNR
spectrumadd=spectrumadd+spectrum*SNR;
end
%% combine the MRS
spectrumadd=spectrumadd/max(abs(spectrumadd));
% noise correction
R = corrcoef(noise_array');
%SNR
maxvalue=max(abs(spectrumadd(round(var_pts/2-200):round(var_pts/2+200))));
noise=std(real(spectrumadd(1:(var_pts*noise_region))));
SNR=maxvalue/noise*0.655;
disp(strcat('combined ','noise:',num2str(noise),' snr:',num2str(SNR)));

% All channels combined time domain FID
Fidadd=ifft(ifftshift(fliplr(spectrumadd)));
figure;
plot(linspace(0,at,var_pts),real(Fidadd));
xlabel('time');
title(strcat(file,'combined'),'Interpreter', 'none');
xlim([0 at]);

% linebroadening unit
lbunit=input('lbunit:');
lbpoint=round(1/(lbunit*at/var_pts)/pi);
% lb
lbaxis=1:var_pts;
Fidaddlb=exp(lbaxis/-lbpoint).* Fidadd;
lbspectrum=fliplr(fftshift(fft(Fidaddlb)));

% renormailed after lb
lbspectrum=lbspectrum/max(abs(lbspectrum));
% plot the lb combined MRS
figure;
plot(faxis,real(lbspectrum));
xlabel('ppm');
title(strcat(file,'combined'),'Interpreter', 'none');
xlim([ppm_left ppm_right]);

% SNR after lb
maxvalue=max(abs(lbspectrum(round(var_pts/2-200):round(var_pts/2+200))));
noise=std(real(lbspectrum(1:(var_pts*noise_region))));
SNR=maxvalue/noise*0.655;
disp(strcat('combined_afterlb','noise:',num2str(noise),'
snr:',num2str(SNR)));

%% 1 order phase correction
a0=0;
fig2=figure;
```

```
plot(faxis,real(lbspectrum));
xlabel('ppm');
title('combined MRS after phasing')
xlim([ppm_left ppm_right]);
% xlim([ppm_left ppm_right]);

uicontrol('Style', 'slider',...
        'Min',-0.8,'Max',0.8,'Value',0,...
        'Position', [500 10 200 20],...
        'Callback', {@replot1,lbspectrum,fig2,faxis,a0});
disp('Once the 1order correction value is chosen, press enter and type in the
a1 value');
pause;

% baseline correction
a1=input('a1:');
disp('baseline correction');
% 1st order phasing correction value
lbspectrumphasing=(lbspectrum.*exp(1j*(a1*faxis+a0)))';
dfaxis=faxis(2)-faxis(1);
lbspectrumphasing = bf(lbspectrumphasing(var_pts/2-
round(10/dfaxis):var_pts/2+round(ppm_right/dfaxis)));

figure;
plot(faxis((var_pts/2-
round(10/dfaxis):var_pts/2+round(ppm_right/dfaxis))),real(lbspectrumphasing)/
max(abs(lbspectrumphasing)));
xlabel('ppm');
title('combined lb MRS after phasing and baseline correction')
xlim([ppm_left ppm_right]);
toc

%% output txt file to jmrui
% this output each channels' FID and combined FID after doing 0 order
% phae correction, linebroading not included

% for i=1:num_ch
% fileID = fopen(strcat(file,'_c',num2str(i),'.txt'),'w');
% fprintf(fileID,'DatasetsInFile: 1 \r\nSamplingInterval: %d
\r\n\r\n',at/length(FID_array(i,:))*1000);
% formatSpec='%d %d\r\n';
% fprintf(fileID,formatSpec,[real(FID_array(i,:));imag(FID_array(i,:))]);
% fclose(fileID);
% end
```

APPENDIX B

VITA

Minyu Gu was born in Shanghai, China in 1994. He received his Bachelor of Science degree in Applied Physics from Tongji University in 2016 and expected to graduate from Master of Science degree in Electrical Engineering from Texas A&M University in 2019. His research interests include Nuclear Magnetic Resonance and Electromagnetism.

Minyu Gu may be reached via email guminyu94@gmail.com.